SGG·SGS **sc | nat** 🇨🇭

Swiss Journal of Geosciences

ORIGINAL PAPER

Open Access

Check for updates

Postglacial evolution of Lake Constance: sedimentological and geochemical evidence from a deep-basin sediment core

Sebastian Schaller[1]* 🔟, Michael E. Böttcher[2,3,4], Marius W. Buechi[1], Laura S. Epp[5], Stefano C. Fabbri[1], Natacha Gribenski[1], Ulrich Harms[6], Sebastian Krastel[7], Alina Liebezeit[2,3], Katja Lindhorst[7], Hanna Marxen[1], Ulli Raschke[8], David Schleheck[5], Iris Schmiedinger[2], Antje Schwalb[8], Hendrik Vogel[1], Martin Wessels[9] and Flavio S. Anselmetti[1]

Abstract

The modern, over 250-m-deep basin of Lake Constance represents the underfilled northern part of an over 400-m-deep, glacially overdeepened trough, which reaches well into the Alps at its southern end. The overdeepening was formed by repeated glacial advance-retreat cycles of the Rhine Glacier throughout the Middle to Late Pleistocene. A seismic survey of Lake Constance revealed a Quaternary sediment fill of more than 150 m thickness representing at least the last glacial cycle. The stratified sedimentary fill consists at the base of ice-contact deposits on top of the molasse bedrock, overlain by glaciolacustrine to lacustrine sediments. During the successful field test of a newly developed, mid-size coring system ("HIPERCORIG"), the longest core (HIBO19) ever taken in Lake Constance was retrieved with an overall length of 24 m. The sediments recovered consist of a nearly continuous succession of lacustrine silts and sands including more than 12 m of Late Glacial sediment at the base. 14 lithotypes were identified through petrophysical and geochemical analyses. In combination with a ^{14}C- and OSL-based age-depth model, the core was divided into three main chronostratigraphic units. The basal age of ~ 13.7 ka BP dates the base of the succession back to the Bølling-Allerød interstadial, with overlying strata representing a complete and thick Younger-Dryas to Holocene succession. The sediments offer a high-resolution insight into the evolution of paleo-Lake Constance from a cold, postglacial to a more productive and warmer Holocene lake. The Late Glacial succession is dominated by massive, m-thick sand beds reflecting episodic sedimentation pulses. They are most likely linked to a subaquatic channel system originating in the river Seefelder Aach, which is, despite the Holocene drape, still apparent in today's lake bathymetry. The overlying Holocene succession reveals a prominent, several cm-thick, double-turbiditic event layer representing the most distal impact of the Flimser Bergsturz, the largest known rockslide of the Alps that occurred over 100 km upstream the river Rhine at ~ 9.5 ka BP. Furthermore, lithologic variations in the Holocene succession document the varying sediment loads of the river Rhine and the endogenic production representing a multitude of environmental changes.

Keywords: Lake Constance, Lake sediments, Rhine glacier, Overdeepening, Subaquatic channels, Flimser Bergsturz

---

1 Introduction

1.1 Background and motivation

Since the beginning of the Quaternary, the Alpine glaciers advanced at least 15 times into the northern Alpine foreland (Keller & Krayss, 2011; Preusser et al., 2011), including the modern area of trinational Lake Constance

🌲 **Springer** Open

(Switzerland, Austria, Germany; Fig. 1). The impact of glaciers on the Alpine landscape and societies triggered in the early nineteenth century first scientific observations. A concise summary of the Quaternary glacial history and its investigation was provided in Preusser et al. (2011). Furthermore, new age constrains on glacial activities during the past glacial cycles correlate well with the evolution of the landscape (Buechi et al., 2018; Gaar et al., 2019). The last and best preserved major glacial advance into the northwestern Alpine foreland (Last Glacial Maximum; LGM) started at ~29 ka BP and reached its maximum extent at ~26–22 ka BP (Gaar et al., 2019). Glaciers retreated back into the Alps at ~18–17 ka BP (Gaar et al., 2019; Ivy-Ochs et al., 2008) and left a perialpine scenery shaped by glacial erosion and deposition. One of the most impressive large-scale erosional features is the creation of widespread glacial overdeepened valleys and basins defined as the topography below the fluvial base level (Buechi et al., 2018; Preusser et al., 2010). The erosional mechanism and processes that control the shape and dimension of these valleys are still widely debated (i.e., Herman et al., 2011; Huuse, 2000; Magrani et al., 2020; Preusser et al., 2010; Reber & Schlunegger, 2016). They initially form proglacial lakes during the glacier's retreating phase that might eventually be filled with lacustrine and (glacio-) fluvial sediments. Some of these initially formed lakes might exist for a long time, such as Lake Constance.

The modern basin of Lake Constance represents a major overdeepened trough in the northern Alpine foreland (Fig. 1). The lake was formed after the retreat of the Rhine Glacier and was initially much larger extending far into the Alps (Keller et al., 2005a, 2005b; Wessels, 1998a, 1998b; Wessels et al., 2015). Lake Constance, together with Lake Walen, Lake Zurich, and others, represents the distal parts of the overdeepenings that have not yet been filled. Previous studies investigating Lake Constance's sedimentological history can be divided into two types: (i) short-core studies using manual coring techniques focusing on the youngest history (e.g., Wessels et al., 1999); and (ii) long-core studies using up to 10 m long cores focusing mainly on the older Holocene and the Late Glacial sediments (e.g. Hanisch et al., 2009; Schneider et al., 2004; Schwalb et al., 2013; Wessels, 1995, 1998b, 1998c). However, the Late Glacial sediments were recovered to date only as a few meters of stratigraphically heavily condensed sediments offering thus only low temporal resolution. This is related to the large water depths (>200 m) and coring techniques, which do not allow to take long (>10 m) cores without mobilizing large drilling
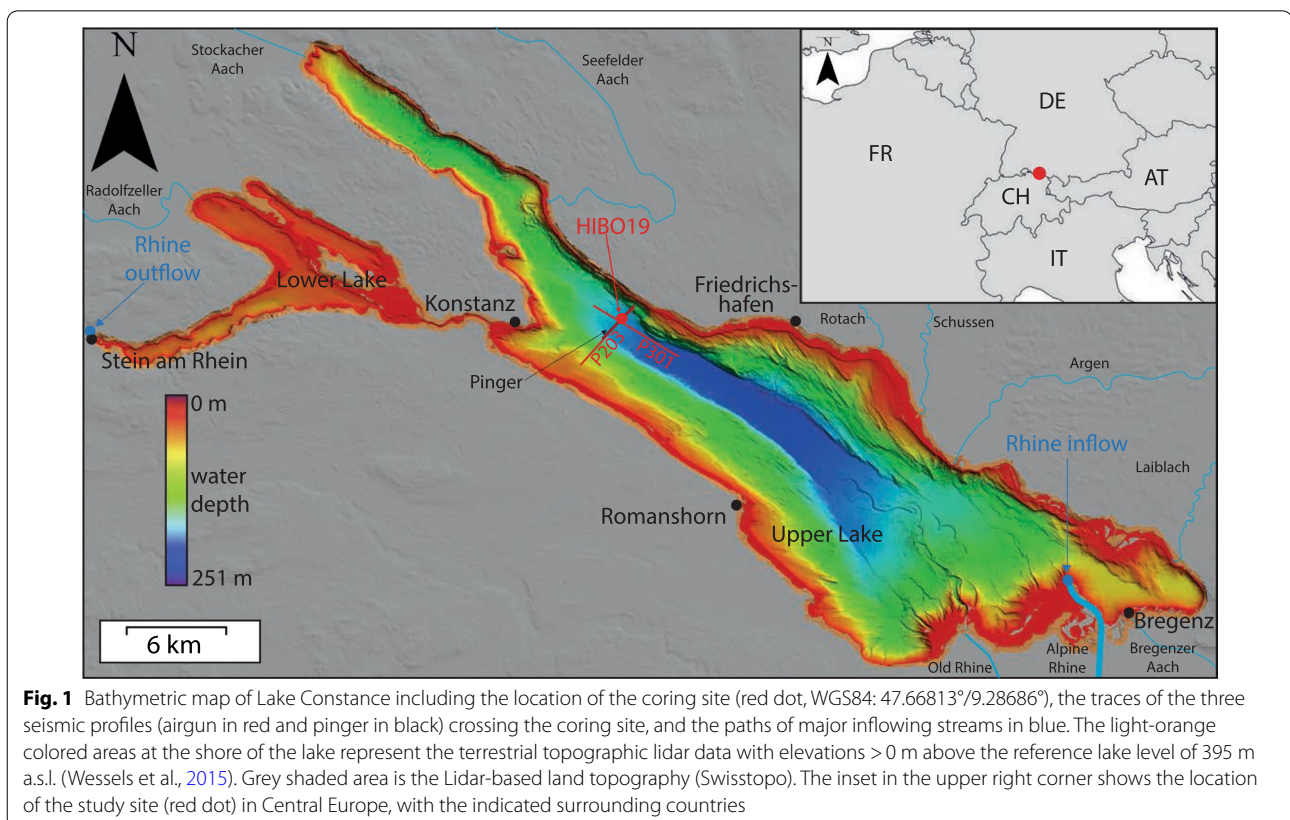
Fig. 1 Bathymetric map of Lake Constance including the location of the coring site (red dot, WGS84: 47.66813°/9.28686°), the traces of the three seismic profiles (airgun in red and pinger in black) crossing the coring site, and the paths of major inflowing streams in blue. The light-orange colored areas at the shore of the lake represent the terrestrial topographic lidar data with elevations >0 m above the reference lake level of 395 m a.s.l. (Wessels et al., 2015). Grey shaded area is the Lidar-based land topography (Swisstopo). The inset in the upper right corner shows the location of the study site (red dot) in Central Europe, with the indicated surrounding countries

equipment. New coring technology became available through the HIPERCORIG coring system (Harms et al., 2020), which bridges the gap between costly deep drilling systems and small manual coring systems. A field test of this coring system (Harms et al., 2020), in combination with new bathymetric (Wessels et al., 2015) and seismic data (Fabbri et al., 2021) of the lake basin (Figs. 1 and 2), offered a unique opportunity to access the deeper

and older lake sediments revealing new insights into the postglacial history of the lake (Harms et al., 2020). This study investigates the pre-Holocene sediments from the deep basin of Lake Constance that were recovered with high-resolution during the HIPERCORIG field-test. Our investigations focus on the lithology, stratigraphy, chronology, and depositional mechanisms providing new implications on pre-Holocene deep lacustrine sediment
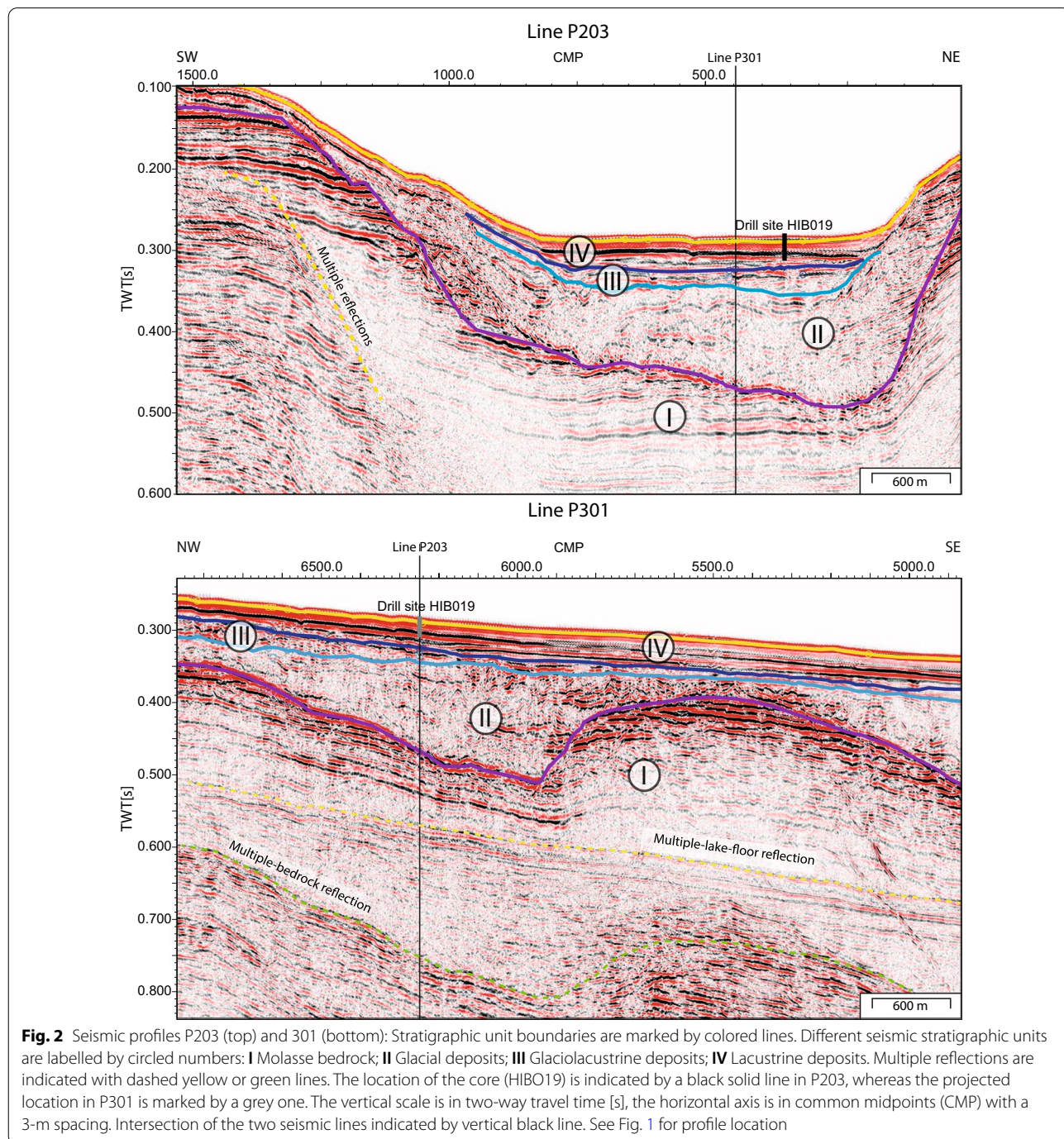
Fig. 2 Seismic profiles P203 (top) and 301 (bottom): Stratigraphic unit boundaries are marked by colored lines. Different seismic stratigraphic units are labelled by circled numbers: **I** Molasse bedrock; **II** Glacial deposits; **III** Glaciolacustrine deposits; **IV** Lacustrine deposits. Multiple reflections are indicated with dashed yellow or green lines. The location of the core (HIBO19) is indicated by a black solid line in P203, whereas the projected location in P301 is marked by a grey one. The vertical scale is in two-way travel time [s], the horizontal axis is in common midpoints (CMP) with a 3-m spacing. Intersection of the two seismic lines indicated by vertical black line. See Fig. 1 for profile location

successions in the context of the glacial retreat as well as the postglacial evolution of the lake.

1.2 Study site

Modern Lake Constance (9°30′ E, 47°30′ N) is a monomictic and oligotrophic lake with a surface of 536 km^2, a maximum water depth of 251 m, and an estimated water volume of ∼50 km^3 (Fig. 1). The reference lake level lies at 395 m above sea level (a.s.l.) with seasonal variations of ±1.5 m. The catchment area of ∼11,500 km^2 is mainly based in the Alps and the surrounding foreland. The main inflow (∼64%, 7.66 km^3/year) is the Alpine Rhine (Schwalb et al., 2013; Wessels, 1998a), while the outflow is the Lower Rhine at Stein am Rhein (Fig. 1). The larger Upper Lake ('Obersee') and the smaller Lower Lake ('Untersee') are connected over the so-called 'Lake-Rhine' ('Seerhein') at Konstanz. The modern lake basin (Fig. 1) represents the remains of an overdeepened valley in the molasse bedrock formed by the Rhine Glacier. The bedrock overdeepening and its sedimentary filling represents the development of the basin since the local LGM-advance that started at ∼29 ka BP when the glacier (partly) re-excavated/eroded the basin. The Rhine Glacier retreated into the Alpine valleys by ∼17 ka BP (Gaar et al., 2019) when the lake became ice-free and first glaciolacustrine and later lacustrine sediments were deposited (Wessels, 1998b). The Late Glacial and Holocene evolution of Lake Constance has been investigated with several up to 10 m long sediment cores (Wessels, 1995, 1998b, and references therein). However, it remains unclear whether deposits from older glacial cycles are preserved in the basin as the deeper sedimentary strata was not recovered to date.

2 Methods

2.1 Bathymetric and seismic data

High-resolution bathymetric data of Lake Constance were acquired in 2013 by a multibeam echosounder survey in deeper waters and by an airborne light detection and ranging (LIDAR) survey in shallow-water areas (Wessels et al., 2015). The resulting bathymetric grid has a cell size of 3 m and covers the entire lake from the Rhine inflow in Bregenz to the outflow in Stein am Rhein. About 500 km of seismic profiles were acquired during multichannel reflection seismic survey campaigns using Mini GI (0.1 l volume) and GI 210 air guns (0.7 l volume) in 2016 and 2017, respectively (Fig. 2). Streamer lengths between 50 and 87.5 m (32–56 channels) were used depending on water depth (shallow Untersee vs. deep Obersee) and available space for maneuvering. Standard processing was carried with a bin distance of 2–3 m (see Fabbri et al. (2021) for details). Vertical resolution of the data is 2–3 m. For time-to-depth conversion of the

airgun seismic data, a velocity of 1600 m/s was assumed for the entire thickness of the Quaternary deposits. In 2021, a cross line was acquired exactly over the drill site with a 3.5 kHz pinger high-resolution single-channel seismic system. These seismic data with a vertical resolution in a dm-scale allow for a detailed core-to-seismic correlation using a constant velocity of 1400 m/s for the uppermost 9 m of unconsolidated water-saturated sediments as determined by matching MSCL-density peaks (see below) with high-amplitude reflections. This velocity is slightly lower than ambient bottom-water velocities (∼1420 m/s at 4 °C) but can be explained by gas-induced sediment expansion after core recovery and by pressure release. All seismic data were interpreted in Kingdom-Suite software.

2.2 Coring operations HIPERCORIG

During the HIPERCORIG-project, a field test for a newly developed medium-size deep-water drilling system took place from May to July 2019 in Lake Constance (Harms et al., 2020). Two drill cores, HIBO19 Core-A and B, with 22 and 20 m length, respectively, and a short core (Core-C) of ∼1.5 m length were taken at a water depth of ∼205 m at a location 5 km East of Konstanz (Fig. 1). The distance between holes A, B, and C was ∼10 m. A detailed description of the drilling device, campaign, and core recovery is given in Harms et al. (2020).

2.3 Core sampling and analysis

Density and magnetic susceptibility of each core section were measured using a GEOTEK-multi-sensor-core-logger (MSCL) (Geotek Limited, Daventry, Northants, UK) with a resolution of 5 mm at the Institute of Geological Sciences, University of Bern. Afterwards, the sections were cut and split longitudinally into an archive half for non-destructive analyses and a working half for sampling use. The archive halves were photographed using the GEOTEK Line Scanner and sedimentologically described. A continuous, nearly gap-less composite splice was established using the short core and the two long cores, based on the macroscopic sedimentological descriptions and the petrophysical properties. Depth is addressed as meter composite depth (mcd) when discussing the entire composite section or as cm-section depth (cmsd) when addressing single core sections (a detailed synopsis is provided in Additional file 2: Fig. S1). Furthermore, X-ray computed tomography (CT) scans of four selected representative core sections were taken using a medical X-ray-CT-scanner (Siemens Somatom) at the Institute of Forensic Medicine, University of Bern.

Samples for geochemical analyses were taken based on the composite section with a spacing of 1.5, 10, and 20 cm down to 0.15, 2.05 and below 2.05 mcd,

respectively. Total carbon (TC), nitrogen, and sulfur were measured via elemental analysis (CHNS elemental analyzer; EuroEA 3052 EuroVector; Lipka et al., 2018). Total inorganic carbon (TIC) was analyzed via an multi element EA 2000CS or a Macro-Element analyzer multi EA 4000CS BU (Analytik Jena; Lipka et al., 2018), or using a Thermo Finnigan MAT 253 gas mass spectrometer coupled to a Thermo Electron Gas Bench II via a Thermo Electron Conflo IV split interface (Böttcher et al., 2018). For the latter measurements, solid $CaCO_3$ and Li_2CO_3 and liquid $NaHCO_3$ standards were used to scale the mass 44 measurements to TIC contents. Total organic carbon (TOC) was derived from the difference between TC and TIC. Weight-percent of carbonates ($CaCO_3$) and organic matter were calculated using a stoichiometrically simplified approach from TIC and TOC through multiplication with 8.3 and 1.8, respectively (Meyers & Teranes, 2001). This approach does not consider potential downcore changes in carbonate phases but allows a 100% sum-curve of lithologic constituents to be calculated. On filtered (0.45 µm cellulose acetate filters) acid extracts (0.5 M HCl for 1 h at room temperature) made on 52 samples taken throughout the entire sediment record, Ca and Mg were measured via ICP-OES (iCAP 7400 DUO, Thermo Fisher Scientific). The Cc/Dol ratios was calculated assuming the earth alkaline elements to be solely bond to calcite, aragonite, or dolomite. 'Cc' stands for the sum of calcite and aragonite, and 'Dol' for detrital stoichiometric dolomite.

Biogenic silica (bSi) concentrations were inferred by means of Fourier transform infrared spectroscopy (FTIRS) at the Institute of Geological Sciences, University of Bern, following the procedures described in Vogel et al. (2016) and using the calibration introduced by Meyer-Jacob et al. (2014). Samples from 0 to 12 mcd were freeze-dried, powdered, and homogenized with an agate mortar and pestle. Further on, 11 mg of the sample were diluted using 500 mg spectroscopic grade and IR transparent potassium bromide (KBr). Sample-KBr mixtures were carefully homogenized and measured on a Bruker Vertex 70 equipped with an HTS-XT multisampler accessory. Siliciclastic content was calculated by subtracting carbonate, organic matter, and bSi content from 100%. Scanning-X-ray fluorescence analysis (scanning-XRF) was performed at 5 mm integrals with an integration time of 20 s using an ITRAX XRF-core scanner (Cox Ltd.) equipped with a Cr-tube set to 30 kV and 50 mA at the Institute of Geological Sciences, University of Bern. Scanning-XRF was employed to investigate relative element concentration changes along the cored sediment succession. An Argon-threshold of >11,200 counts was used to filter out low-quality data caused by gaps, cracks, and surface roughness (e.g., coarse sands). Based on all

analyses and additional smear slide microscopic observations, seven background (Table 1) and seven event lithotypes (Table 2) were determined and described. Furthermore, the cored succession was divided into three main lithostratigraphic units.

Additionally, the prominent event layers at 8.89–9.02 mcd were divided into 1 and 0.5 cm thick intervals, respectively, on which the grain-size distribution, the mineral-phases composition, and the lithological constitution were determined. The high-resolution semi-quantitative grain-size laser-diffraction analysis (Taubner et al., 2009) was conducted at the Institute of Geography, University of Bern, using a Malvern Mastersizer 2000. These samples were treated with a dispersion agent (11 g/l $(NaPO_3)_6 + 2.3$ g/l Na_2CO_3) overnight to separate the small grain-size fractions. For determining the mineral-phase compositions via Powder X-ray Diffraction (PXRD), a mixture of 4 g sample, 1 g corundum (internal standard) and 10 ml Ethanol were homogenized for 6 min in a Mccrone Mill (Retsch). After drying, the powder was measured with an Empyrean diffractometer from Malvern Panalytical using a Cu X-ray source (40 kV, 40 mA), fixed divergence slit (0.25°) and a 1Der detector (Malvern Panalytical), from 5 to 75° 2Θ with an integration time of 0.8 s per step with a step size of 0.017° 2Θ. Quantification was done in TOPAS ACADEMICS V6 (Coelho Software) using Rietveld refinement. Clay phases were fitted by the Pawley method and quantified via the internal standard (e.g., Akker et al., 2021). All PXRD measurements were done at the Institute of Geological Sciences, University of Bern. The lithological constitution is based on the same method as described above for the entire core, except that bSi was not measured for these samples.

2.4 Chronostratigraphy and age model

The chronostratigraphic model is based on a combination of seven radiocarbon (^{14}C) ages and three optically stimulated luminescence (OSL) ages as well as the correlation of a prominent turbidite layer (Schneider et al., 2004) with the previously ^{14}C-dated Flimser Bergsturz (Deplazes et al., 2007). Tephra-bearing horizons (i.e., Laacher See tephra) could not be identified upon macroscopic core description. All ages were obtained from samples collected below 8.83 mcd, as the focus of the study is laid on the lower section.

To obtain the radiocarbon samples, sediments were sieved to extract macroscopic terrestrial organic remains. The samples were cleaned and, if possible, identified, small samples were merged (Table 3). ^{14}C-data were acquired with accelerator mass spectrometry (AMS) at the LARA laboratory, University of Bern. ^{14}C-ages were calibrated using OxCal and the IntCal20 calibration

Table 1 Description and interpretation of background lithotypes with photo of original core section (origin of line scan is indicated in the lower right corner of core photos, scale is in cm)

Background lithotypes

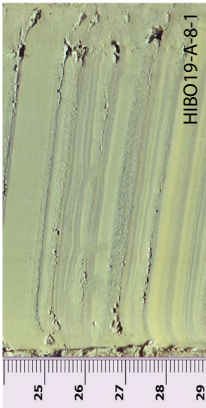| Description	Interpretation	Core photo
LB1: light to dark grey, partly black, mostly finely laminated (< 1 mm) to laminated (< 5 mm) silty mud. Sporadic cm-scale black and slightly coarser layers with a brighter top. Increased bSi- (up to 7%) and organic matter-content (up to 3%), and variable $CaCO_3$-content (~ 30–50%)	Finely laminated varves, thickness changes due to variable runoff. Allochthonous origin of carbonates dominates over the insitu chemical/biological induced production. Black colour and higher organic matter- and bSi-concentrations are linked with eutrophication and iron-sulphide formation. Deposited in deep water, low-energy, and reducing conditions	HIBO19-C-1-1
LB2: light to dark grey, mostly laminated (< 5 mm) to finely laminated (< 1 mm) silty mud. Few cm-scale dark and slightly coarser layers with a brighter top. Very low bSi- (< 1%) and organic matter-content (~ 1%), and $CaCO_3$-content ~ 20–30%	Finely laminated varves, thickness changes due to variable runoff. Allochthonous origin of carbonates dominates strongly over the insitu chemical/biological induced production. Deposited in deep water and low-energy conditions	HIBO19-C-1-1
LB3: light to dark grey mottled clayey silt. Some scattered laminae. Dots and smears may indicate original layering	Disturbed sediments; drilling artefact. Mainly top and bottom parts of the core sections are affected	HIBO19-B-1-2
LB4: mainly finely laminated to partly layered grey to beige-grey silty mud. Very low bSi- (< 1%) and organic matter-content (~ 1%). $CaCO_3$-content of ~ 25–30%	Finely laminated varves, thickness changes due to variable runoff. The increased concentration of allochthonous carbonates indicates rapid clastic deposition that may be correlated to increased sediment flux. Deposited in deep water and stable low-energy conditions	HIBO19-A-3-1

Table 1 (continued)

Background lithotypes

Description	Interpretation	Core photo
LB5: mainly finely laminated to partly layered grey to beige silty mud. Very low bSi- (< 1%) and organic matter-content (~1%). $CaCO_3$-content ~45–50%	Finely laminated varves, thickness changes due to variable runoff. Carbonates are mainly product of bio-chemical-induced precipitation. Deposited in deep water and stable low-energy conditions	HIBO19-A-4-2
LB6: mostly homogeneous, partly laminated beige to grey-beige silty mud. Very low bSi- (< 1%) and organic matter-content (< 1%). $CaCO_3$-content ~25–30%	Dominated by clastic sedimentation. The more homogeneous parts were deposited in stable and rather low-energy conditions, with low sedimentation rate. The more heterogeneous parts were deposited in more unsteady energy conditions with a more variable sedimentation rate	HIBO19-A-5-1
LB7: mainly finely laminated to partly layered alternating grey-beige and yellowish-beige clay. No traceable bSi- and organic matter content. Average $CaCO_3$-content ~30%	Background sediment deposited during the inactive phases of the subaquatic channel. The varves are interpreted as alteration of aeolian transported loess deposits and clastic sedimentation. Thickness changes due to variable runoff. Deposited in deep water and stable low energy conditions (Niessen et al., 1992; Wessels, 1995, 1998a, 1998b, 1998c)	HIBO19-A-8-1

Table 2 Description and interpretation of event lithotypes including photo of core section (origin of line scan is indicated in the lower right corner of core photos, scale is in cm). Yellow double arrows indicate the vertical extent of described event layer
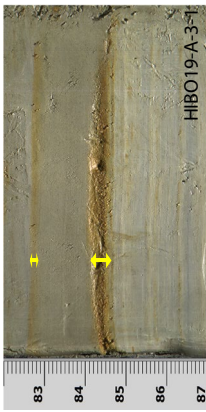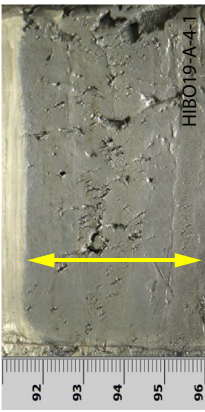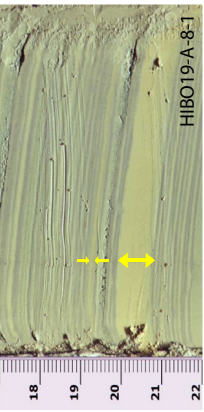
Event lithotypes

Description	Interpretation	Core photo
LE1: mm-scaled coarser oxidized sandy layers and patches. These layers occur at the base of fining upwards event layers or isolated	Rusty colour indicates high concentration of iron-sulphide minerals. Minerals may be of allochtonous origin (event deposits) or more likely of post depositional origin, in particular in the isolated finer layers and patches. Not clear, if oxidation was pre- or post-drilling	HIBO19-A-3-1 83 84 85 86 87
LE2: fining upwards brown to grey-brown layers at cm-scale with occasional wavy structures and slight brightening towards top. Sometimes base with initial coarsening-upward trend. Layers with gentle erosive basal contact. One prominent layer (8.9–9.02 mcd) reaches a thickness of ~10 cm. Maximum grain size reaches up to middle sand in the thickest layer, otherwise silt to maximal fine sand	Turbiditic event deposit, thickness variation due to the intensity and distance to the event. Lack of coarser grains at the base hints to a more distal source. The colour indicates an allochtonous source rather than remobilised lake deposits. The waving and graded internal structure hints towards a slow-event deposition under rarely increasing and the decreasing energy condition, typical for flood events	HIBO19-A-4-1 92 93 94 95 96
LE3: grey to dark grey silt layers at a mm to cm-scale. Homogeneous darker lower part, with a fining upwards and brightening-up top part. With a partly erosive basal contact	Turbiditic event deposit, variation in thickness is related to the size and distance to the event. Lack of coarser fractions at the base hints towards a distal source. The mostly homogeneous structure and bright clay caps indicate a fast deposition, typical for mass movement deposits, and therefore mainly remobilised lake-sediments	HIBO19-A-5-1 78 79 80 81 82
LE4: structureless bright yellowish-beige clay layers in a mm- to cm-scale	Interpreted as aeolian transported loess deposits, colour change may indicate a difference origin of the loess or a higher concentration then in LB7 (Niessen et al., 1992; Wessels, 1995, 1998a, 1998b, 1998c)	HIBO19-A-8-1 18 19 20 21 22

Table 2 (continued)
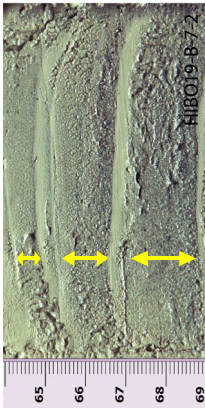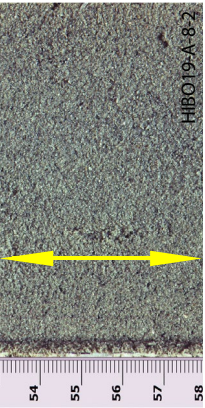
Event lithotypes

Description	Interpretation	Core photo
LE5: mud-clast conglomerate: mixture/melange of beige fine- to middle-sand, with beige silty mud-, yellowish-beige clay-, and grey clay-clasts. With an average $CaCO_3$-content of ~ 30%	Mass movement deposit formed in subaquatic channel	
LE6: Fining-upward dark grey to brownish fine- to occasionally middle-sand sequence. Thickness of individual sequences in a mm- to dm-scale. Occasionally, high concentration of terrestrial organic material and/or a high mica concentration in the fine fraction. Average $CaCO_3$-content (15–20%)	Distal subaquatic channel deposits, the fining upward sand sequences represent the active states of the channel. The thickness of the sand-sequences is controlled by the size and the distance of the event. The terrestrial material in the sand sequences indicates at least partly terrestrial sand source. Deposited in deep water and medium- to high-energy conditions	
LE7: massive unstructured dark grey to brownish middle- to coarse-sand. Thickness of individual layers range from dm- to m-scale. Average $CaCO_3$-content (15–20%)	Proximal main subaquatic channel deposits, each graded sequence represents a single event. Deposited under deep-water and high energy conditions	

Table 3 Radiocarbon age data

Radiocarbon measurements

Sample	Core-section	Section depth [cmsd]	Composite depth [mcd]	Age uncalibrated [yr BP]	Lab code	Age calibrated [yr BP]	Material
14C-1[a]	HIBO19-A-4-1	85–87	8.83–8.85	8322 ± 90	BE-14442.1.1	9525–9029	Young branches + bud scale
14C-2[a]	HIBO19-A4-2	5–15	9.02–9.12	8434 ± 190	BE-14443.1.1	10,120–8987	Leaf fragment + undefined terrestrial material
14C-3	HIBO19-A-4-2	66–68	9.63–9.65	9598 ± 40	BE-14444.1.1	11,163–10,763	Needle fragment (Pinus) + bud scale
14C-4[a]	HIBO19-A-5-1	56–58	10.60–10.61	9973 ± 120	BE-14445.1.1	11,878–11,196	Undefined terrestrial seed + 1 seed (Betula)
14C-5	HIBO19-A-5-2	24–25	11.28–11.29	12,294 ± 25	BE-14446.1.1	14,786–14,095	Wood fragment
14C-6[a]	HIBO19-A-10-2	87–88	21.90–21.91	12,409 ± 115	BE-14447.1.1	15,013–14,094	Undefined leaf fragment + piece of bark
14C-7	HIBO19-A-11-2	87–88	23.98–23.99	11,772 ± 70	BE-14448.1.1	13,784–13,496	Branch + 2 seed and leaf (Betula nana) + seed (Caryophyllaceae)
Flimser Bergsturz	HIBO19-A-4-1	91.5–99.5	8.895–9.025			9480–9430	Corelation of turbiditic event layer with Flimser Bergsturz 14C-age (Deplazes et al., 2007)
	HIBO19-A-4-2	0.5–5					

[a] Marks the CO_2-gas measurements, otherwise measurements were done on graphite

curve (Reimer et al., 2020) and are presented with a 2-σ range.

Three OSL-samples were taken in the coarse sandy facies as whole-core rounds prior to opening to minimize the risk of light penetration and resetting of the natural luminescence signal. Two samples were taken from core sections that are not part of the composite core. These samples depths were projected onto their correlated composite depth by visual matching key lithological features. All further preparations and measurements were done under red-light conditions. The 180–250 μm potassium (K)-feldspar fraction was extracted by using the standard OSL-sample preparation protocol (Preusser et al., 2008). All measurements were conducted using TL/OSL DA-RISØ reader in the Luminescence-Laboratory, University of Bern. A post-IR IRSL 150 protocol (Reimann & Tsukamoto, 2012) was used to measure the equivalent dose (D_e) from two signals measured at 50 °C (IR50) and at 150 °C (pIR150). Dose recovery and residual-dose tests were conducted to check the reliability of the protocol, with recovered dose for each sample within 10% of the originally given dose. D_e measurements were done on 24 aliquots of 1 mm diameter for each sample. Measurements for fading-rate estimates were additionally carried out following Auclair et al. (2003). Final D_e per sample for both IR50- and pIR150-signals were calculated using the central age model (CAM; Galbraith et al., 1999). The concentrations of relevant radionuclides (i.e., K, Th, and U) for dose rate (D_r) determination were measured with high-resolution low-level gamma spectrometry at the

LARA laboratory at the University of Bern (Preusser & Kasper, 2001). Water content was determined on the basis of bulk-density MSCL-data (Lukas et al., 2012). Based on these results, the final D_r for each sample was calculated by using the Dose Rate and Age Calculator (DRAC; Durcan et al., 2015). Calculated ages (sample D_e/D_r) were then corrected for fading, using the fading correction model by Huntley and Lamothe (2011) included in the Luminescence R package (Kreutzer et al., 2012).

The age-depth model is primarily based on a second-degree polynomial line regression of the ¹⁴C-ages. The ¹⁴C-ages were selected due to the internal consistence in sampling, measurement, analyses, and error dimension. The best fit and the uncertainty range were manually picked according to the weighted probability, the OSL-ages, and the correlated Flimser Bergsturz-age. The 2-σ probability envelop of the ¹⁴C-ages was also manually modified to include the OSL-ranges.

3 Results

3.1 Seismic data

Seismic data provide an overview of the larger stratigraphic architecture of the study area and helps to understand the major phases in the development of Lake Constance since the last glacial cycle. It reveals a ~200 m deep u-shaped erosional truncation of the bedrock below today's lake floor. The stratified fillings of this incision were interpreted as glacial, fluvial, and lacustrine deposits (Fig. 2). The sedimentary cover on top of the bedrock at the drill site amounts to ~180 ms two-way-travel

time (twt) equaling ∼145 m. Based on the seismic facies analysis of profile P203 and P301 (Fig. 2), four major seismic stratigraphic units were described (Fabbri et al., 2021): Unit I is characterized by horizontally and laterally continuous high-to-medium-amplitude reflections with a sharp erosional upper boundary to the overlying Unit II, and is interpreted as the molasse bedrock. Unit II is characterized by variable thickness (up to ∼140 ms twt = ∼110 m) and by a transparent to chaotic seismic facies with only few non-continuous reflections. This unit is interpreted to represent glacial deposits. Unit III has a maximum thickness of ∼20 ms twt corresponding to ∼15 m and levels out most of the topography. The lower part of Unit III is characterized by rather transparent seismic facies with few continuous reflections, whereas the upper part displays some higher-amplitude horizontal reflections with slightly upwards-bend lateral onlaps onto Unit II. Unit III is interpreted as glacio-lacustrine deposits. The uppermost Unit IV is composed of continuous high-amplitude reflections that mostly drape the underlying strata and that consist of Late Glacial and Holocene lacustrine sediments as confirmed through coring (Hanisch et al., 2009; Schwalb et al., 2013; Wessels, 1995, 1998b).

3.2 Lithotypes

The 24-m-long composite succession was divided into seven lithotypes reflecting background sedimentation (LB1-7), and seven lithotypes reflecting event-deposition (LE1-7) (Figs. 3 and 4). Lithologic descriptions and interpretations of the respective depositional environment as well as representative core-photographs of the lithotypes are provided in Table 1 for LB1-7 and Table 2 for LE1-7. Figure 5 illustrates detailed line scans and CT scans of selected core sections with key lithotypes.

3.3 Age-model

The seven ^{14}C-ages and the published age of the Flimser Bergsturz (Deplazes et al., 2007) are provided in Table 3. Two samples, ^{14}C-5 and ^{14}C-6 were classified as 'reworked', because they show an older age than ^{14}C-7 and they consist of large material that can easily survive reworking processes (driftwood, piece of bark/wood; Table 3). The OSL-ages support this interpretation (Fig. 6 and Table 4): the three OSL-ages overlap within errors, spanning ∼10.9 to ∼14.7 ka BP for the IR50 signal, and ∼11.0 to ∼16.8 ka BP for the pIR150 signal (Additional file 1: Table S1). The IR50-ages were selected for the final chronology as this signal is faster to bleach under light exposure (Colarossi et al., 2015), thus, limiting the risk of inherited signal potentially carried over from previous transport deposition cycles ('partial bleaching'). Such a phenomena is common in fast depositional environments

(López et al., 2018) and may lead to significant age overestimation. However, based on the moderate dispersion (Table 4) of the aliquots D_e-distribution, the general age agreement between both signals (Additional file 1: Table S1), and the radiocarbon-based chronology, no significant partial bleaching is expected for the analyzed samples.

Because this study focusses on the early to pre-Holocene sediments, the refined age model (Fig. 6) starts at a depth of 8.83 m with an age of ∼9.4 ka BP. The transition between Younger Dryas and Holocene is located at ∼11.4 (min 10.3, max 13.8) mcd. The Bølling-Allerød—Younger Dryas boundary is placed at ∼20.35 (min 16.95, max 21.55) mcd. The age-depth model can roughly be divided into three sections with characteristic sedimentation rates: (1) slow deposition between 0 and ∼9.65 mcd, with an estimated sedimentation rate of ∼0.88 m/ka; (2) a transition zone between ∼9.65 and 10.6 mcd with a sedimentation rate of ∼1.9 m/ka; and (3) a zone of fast deposition ∼from 10.6 mcd to the bottom (∼24 mcd) with an estimated sedimentation rate of ∼6.4 m/ka.

3.4 Stratigraphic units and core-to-seismic correlation

Based on the 14 defined background and event lithotypes (Tables 1a and b), the succession (Figs. 3 and 4) was divided into three main stratigraphic units (1, 2, and 3) with Unit 1 containing four subunits (1a–1d). These units are described in detail [incl. age range according to age model (Fig. 6)] from top to bottom in the following section. Additionally, a correlation with the stratigraphic units presented in Wessels (1995, 1998b), Hanisch et al. (2009), and Schwalb et al. (2013) is given in Table 4.

Unit 1 (0 to 9.96 mcd; 0 to ∼11.5 ka BP) Consists of laminated to layered grey (LB1, 2, and 3) to beige (LB 4 and 5) silty mud. The grey variety rather occurs in the upper part, the beige variety in the lower part of the units. These lithologies are intercalated by several types of event layers (LE1, 2, 3, and 6). The low-density values at the very top represent the uncompacted youngest sediments at the lake floor. In the high-resolution seismic data, Unit 1 is characterized by a laterally continuous and rather draping seismic facies with a series of medium-to-high amplitude reflections (Fig. 7). Overall, density values slightly increase downcore. In general, the magnetic susceptibility signal shows low values over the entire Unit 1. Density and magnetic susceptibility signals show matching peaks that are mostly linked to event layers. The very top of Unit 1 is characterized by high bSi and organic matter concentrations, which quickly decrease downcore to a stable lower level for the remaining part of the unit. $CaCO_3$ content shows a variable pattern in the upper half, including a peak with high values at the very top. It reaches a maximum of over 55 wt% in the lower parts of
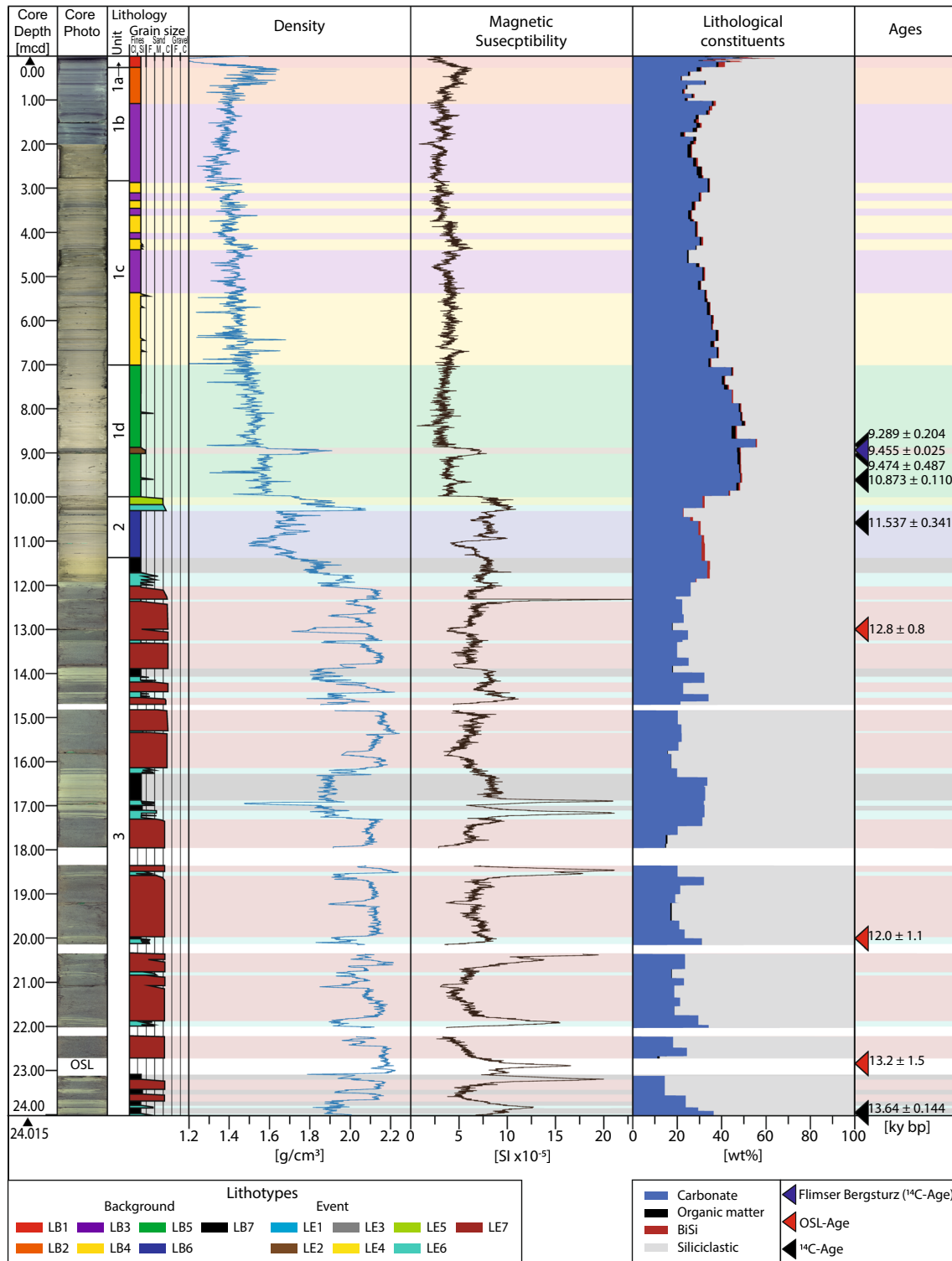
Fig. 3 Petrophysical and lithological data versus depth of the HIBO19 composite core section. Columns from left to right: depth-scale [mcd], combined composite core photo (line scan), stratigraphic units (labelled with numbers), lithotypes (color code in the lower left corner) with indicated grain size, density [g/cm³], magnetic susceptibility [Si × 10⁻⁵], lithological constituents extrapolated over the whole sample interval [wt%]. Relevant ages for the age-model with the corresponding errors are shown at right side. Lithotypes are shown as semi-transparent color codes over the plot's entire width. Gaps in the cores are indicated in white. The lowermost gap is caused by whole-core OSL-sampling leaving only MSCL-data available for this section
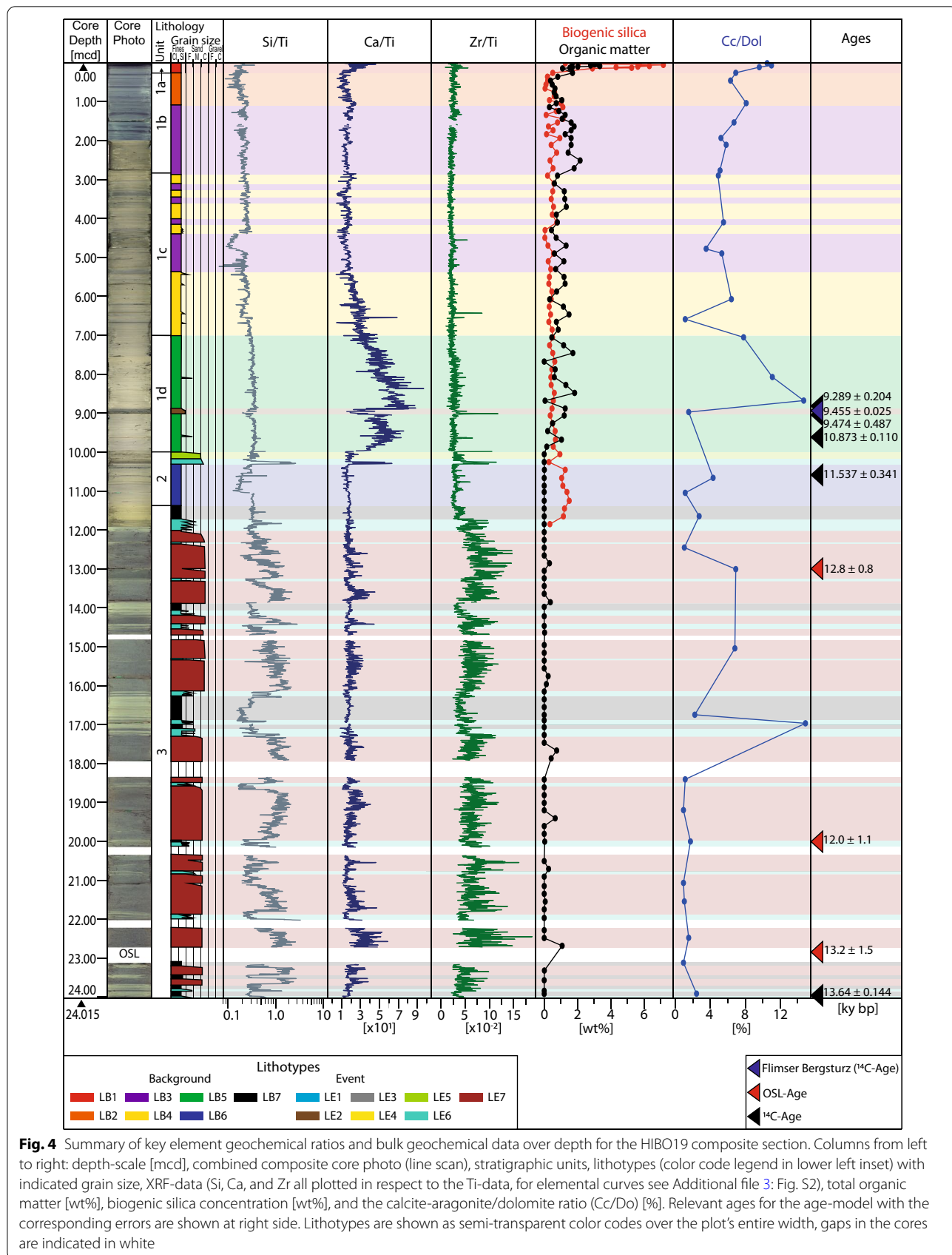
Fig. 4 Summary of key element geochemical ratios and bulk geochemical data over depth for the HIBO19 composite section. Columns from left to right: depth-scale [mcd], combined composite core photo (line scan), stratigraphic units, lithotypes (color code legend in lower left inset) with indicated grain size, XRF-data (Si, Ca, and Zr all plotted in respect to the Ti-data, for elemental curves see Additional file 3: Fig. S2), total organic matter [wt%], biogenic silica concentration [wt%], and the calcite-aragonite/dolomite ratio (Cc/Do) [%]. Relevant ages for the age-model with the corresponding errors are shown at right side. Lithotypes are shown as semi-transparent color codes over the plot's entire width, gaps in the cores are indicated in white

Fig. 5 CT and line scans of selected representative core sections of HIBO19. Each core section is labelled at the top, scale is in cm, each column shows from left to right: line scan, corresponding CT scan, and lithotypes. The color code for the lithotypes is given at the bottom right. Shown core-sections from left to right: Surface core (13–114 cm → 0–1.01 mcd), A-3-1 (61.5–100.5 cm → 6.19–6.58 mcd), B-5-2 (23.5–80.0 cm → 9.96–10.53 mcd), B-8-2 (0.5–75 cm → 15.8–16.545 mcd). A detailed graphical synopsis of the depth conversion of all sections, section parts included in the composite section, and the corresponding composite depth is provided in Additional file 2: Fig. S1
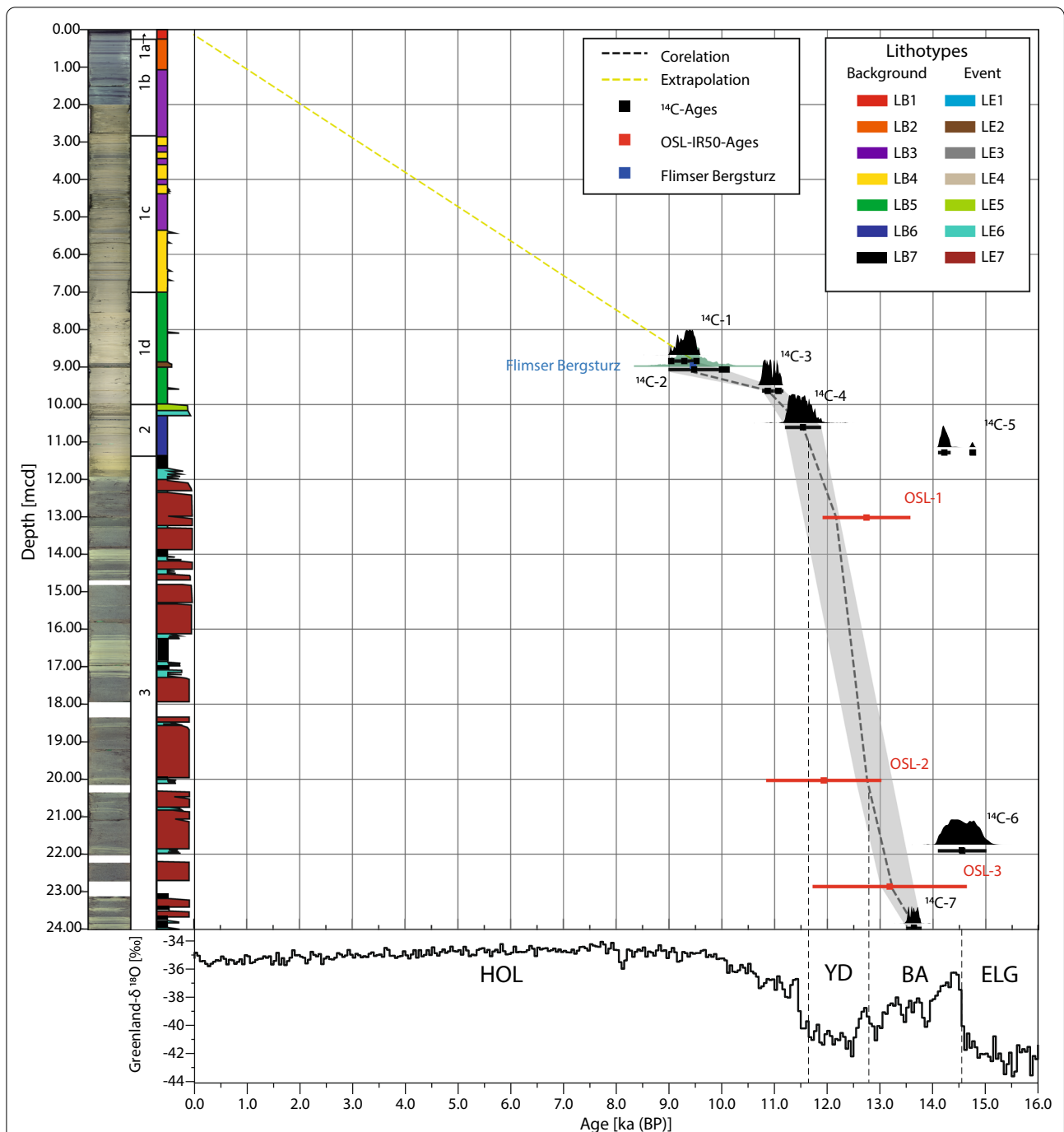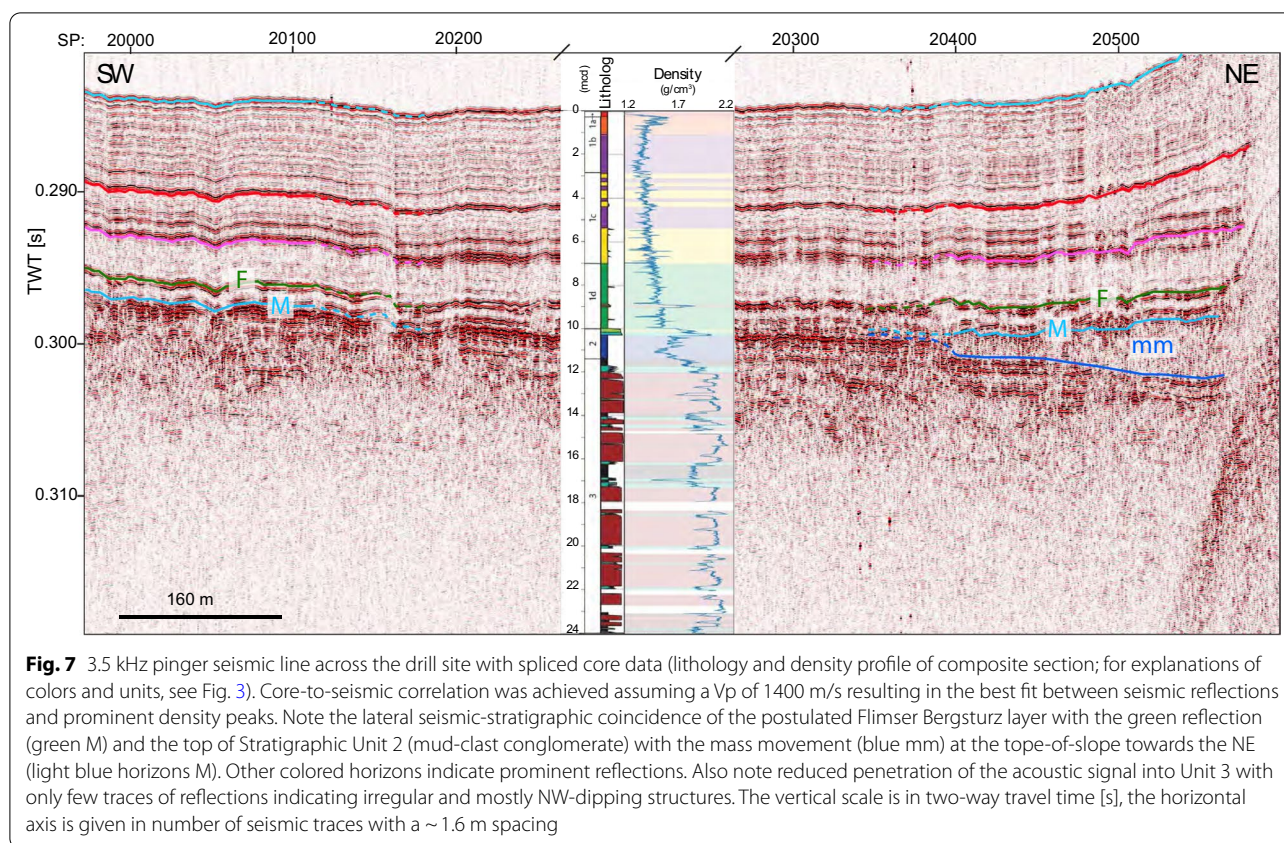
Fig. 6 Age-depth model of HIBO19 composite section. The ages are given in ka BP and marked with squares. Uncertainties are indicated by x-axis error-bars: ^{14}C (black, 2σ-range); OSL-IR50 (red, gaussian approach); Flimser Bergsturz correlating (blue, given uncertainty). Depth scale in meter composite depth, the marker-size exceeds the depth-interval of the samples. The probability histograms for the ^{14}C-ages are given above the corresponding calibrated ages in black and for ^{14}C-2 in semi-transparent green. The age-depth correlation below 8.83 mcd is indicated by a black dashed line, above, the model was just extrapolated with a straight line (yellow dashed line). The probability envelope is indicated in grey. The δ^{18}0 data in [‰] (National Centers for Environmental Information (NCEI), 2020) from 0 to 16 ka BP as a global temperature proxy with the geochronological ages are plotted below: Hol, Holocene; YD, Younger Dryas; BA, Bølling–Allerød; ELG, Early late Glacial. The boarders are extrapolated with vertical black dashed lines into the age-depth model. The combined composite photo, the stratigraphic units, and the lithotypes with the estimated grain size are given on the left side

Table 4 OSL-IR50 age data

OSL-IR50 measurements

Sample	Core-section	Section depth [cmsd]	Composite depth [mcd]	De [Gy]	K [%]	U [mg/kg]	Th [mg/kg]	Water cont. [wt. %]	Over disp. [%]	g-valuemean ± std. [%]	Dr [Gy/ka]	Age [ka BP]	Litho-type
OSL-1	HIBO19-B-7-1	20–27	12.98–13.05	28.2 ± 0.57	1.15 ± 0.01	2.39 ± 0.14	4.08 ± 0.15	20 ± 5	9.6	1.83 ± 0.07	2.57 ± 0.16	12.8 ± 0.8	LE7
OSL-2	HIBO19-B-10-2	21–28	19.99–20.06	23.4 ± 1.20	0.92 ± 0.01	2.28 ± 0.16	3.56 ± 0.07	19 ± 5	24.9	2.01 ± 0.34	2.32 ± 0.15	12.0 ± 1.1	LE7
OSL-3	HIBO19-A-11-1	70–79	22.82–22.91	29.5 ± 0.70	0.88 ± 0.01	3.51 ± 1.57	2.67 ± 0.11	16 ± 5	11.3	1.53 ± 0.03	2.54 ± 0.27	13.2 ± 1.5	LE7

The Lithotype code from Table 2 contains the information for the depositional environment. K, U, Th, and water contend were used for dose-rate calculations. The overdispersion is important for partial bleaching estimations, whereas the g-values are important for the fading correction, an expanded table with the complete OSL-data is given in the Additional file 1: Table S1

Fig. 7 3.5 kHz pinger seismic line across the drill site with spliced core data (lithology and density profile of composite section; for explanations of colors and units, see Fig. 3). Core-to-seismic correlation was achieved assuming a Vp of 1400 m/s resulting in the best fit between seismic reflections and prominent density peaks. Note the lateral seismic-stratigraphic coincidence of the postulated Flimser Bergsturz layer with the green reflection (green M) and the top of Stratigraphic Unit 2 (mud-clast conglomerate) with the mass movement (blue mm) at the tope-of-slope towards the NE (light blue horizons M). Other colored horizons indicate prominent reflections. Also note reduced penetration of the acoustic signal into Unit 3 with only few traces of reflections indicating irregular and mostly NW-dipping structures. The vertical scale is in two-way travel time [s], the horizontal axis is given in number of seismic traces with a ~1.6 m spacing

the unit and then quickly decreases at the very bottom of Unit 1. The Cc/Dol ratio lays between 16 and 2, follows qualitatively the $CaCO_3$-pattern. The Ca/Ti-ratio reveals matching patterns with the $CaCO_3$ content supporting its function as indicator for endogenic calcite abundance (Croudace & Rothwell, 2015). The Si/Ti and Zr/Ti ratios, serving in this study as indicators for greater grain sizes (Croudace & Rothwell, 2015), are low with some minor peaks. They match with the density and the magnetic susceptibility signals as well as with the estimated grain size of the background sediments and the event layers.

Subunit 1a (0–0.24 mcd) The uppermost sediments below the lake floor consist of light grey to black (thin) laminated silty mud (LB1) as exemplified in the very top of the surface core (Fig. 5). The topmost ~1–2 cm were remobilized during the drilling process. The whole Subunit 1a shows low density and magnetic susceptibility values that correspond with the high contents in bSi, organic matter, and $CaCO_3$, as well as with the high Cc/Dol-ratio.

Subunit 1b (0.24–2.86 mcd) Consists of light grey to dark grey (thin) laminated silty mud (LB2) with potential coring artefacts (LB3) as shown in the surface core (Fig. 5). The top of the subunit shows an increased density and magnetic signal, that matches with increased siliciclastic content. The section shows low bSi values as well as downcore increasing organic matter content and decreasing Cc/Dol-ratio. Density and magnetic susceptibility values decrease slightly towards the bottom of Subunit 1b. Due to the coring artefacts, these petrophysical signals might represent rather disturbed signals, hence, no reliable detailed correlations between the measured signals can be established.

Subunit 1c (2.86—gradual transition between 6.75 and 7.25 mcd) This subunit consists of finely laminated to partly layered grey to beige-grey silty mud (LB4) with potential coring artefacts (LB3) as shown in core section A-3-1 (Fig. 5). The background sediments are sporadically intercalated by several types of event layers such as mm-scaled rusty colored laminas (LE1), brownish to grey fining up turbiditic type (LE2), and traces of greyish homogeneous deposits (LE3). There is no systematic correlation between the occurrences of the event layers. The subunit is characterized by rather low density and magnetic susceptibility values. In general, both signals slightly increase downcore, but display an unstable pattern with high amplitudes and high-frequency variations. Some of those minor peaks coincide with identified event deposits (LE2 and LE3). Furthermore, the entire subunit displays very low bSi-, variable low organic-matter-, and medium

CaCO$_3$ contents and Cc/Dol ratio, which are increasing downcore corresponding with the Ca/Ti ratio. Si/Ti and Zr/Ti ratios are low with some minor peaks indicating little grain-size variability.

Subunit 1d (gradual transition between 6.75 and 7.25–9.96 mcd) This subunit consists of finely laminated to partly layered grey to beige silty mud (LB5) that is intercalated by few rusty layers (LE1) and by greyish, more homogeneous layers (LE3) at the transition to Subunit 1c. The lithology of Subunit 1d is shown in the top ~20 cm of core section B-5-2 (Fig. 5). In contrast to the overlying subunits, several sub-cm- to cm-thick fining-up sand layers (LE6) occur. Two prominent brownish fining-up event layers (LE2) occur at 8.895–9.025 mcd; these layers are postulated to be the distal effect of the Flimser Bergsturz (Schneider et al., 2004), and were correlated with an existing ^{14}C-age (Deplazes et al., 2007) (Table 3; see "Discussion" section below). These two stacked layers have sufficient thickness and high density to produce a clear high-amplitude reflection on the high-resolution seismic data (green horizon M; Fig. 7), whereas the remainder of the subunit coincides with a rather transparent seismic facies. In general, the density signal slightly increases from top to bottom of Subunit 1d, whereas the magnetic susceptibility remains low. The subunit is characterized by very low bSi values, oscillating low organic matter, high CaCO$_3$ contents, and high Cc/Dol ratio. The Ca/Ti-ratio correlates well with the CaCO$_3$ contents and the Cc/Dol ratio above the prominent event layer, but below, this correlation is weaker. The Zr/Ti-ratio shows a strong and sharp peak at the prominent event layer and some minor peaks correlating with sandy event layers.

Unit 2 (9.96–11.38 mcd; ~11 to ~12 ka BP) The top ~33 cm (9.96–10.29 mcd) consists of a mud-clast conglomerate (LE5) with a partly erosive fining-up middle sand base (LE6) shown in core section B-5-2 (Fig. 5). This mud-clast conglomerate has strongly elevated density and magnetic susceptibility values when compared to overlaying and underlying lithologies. It coincides in the high-resolution seismic data with a zone of high-amplitude reflections (light blue horizon M; Fig. 7) which was previously identified in other high-resolution seismic surveys in Lake Constance (Schwestermann, 2016). The remaining underlaying part of Unit 2 is built up by homogeneous to laminated beige to grey-beige silty mud (LB6). The more laminated upper part (10.23–11.04 mcd) is intercalated by few cm-scaled homogeneous grey (LE3) and fining-up sand layers (LE6), whereas the homogeneous lower part (11.04–11.38 mcd) contains the uppermost bright yellowish-beige mm-scaled clay layer (LE4). While no traces of organic matter were measured, a slightly increased bSi content is identified. CaCO$_3$ contents of the background sediments increase slightly from top to bottom, whereas the Cc/Dol ratio shows waring values on a rather low level. Ca/Ti, Si/Ti and Zr/Ti ratios display major peaks in the sand succession (Fig. 4).

Unit 3 (11.38–24.015 mcd; ~12 to ~13.5 ka BP) Unit 3 shows a fine (LB7) and a coarse (LE6, LE7) endmember lithology: ~30% of the unit are composed of laminated alternating grey-beige and yellow-beige clay to clayey silt lithologies (LB7), varying between mm thick, isolated laminas, and several dm-thick, nearly continuous beds (i.e., ~11.4 to ~11.6 and ~16.3 to ~16.9 mcd). These clay-rich successions are either interrupted by thinly laminated to bedded fining-up sandy successions (LE6) or by fining-up sandy successions followed by massive sand beds (LE6+LE7), making up ~70% of the units. The high-resolution seismic signals did not fully penetrate Unit 3, as only minor traces of reflections can be recognized on the seismic line (Fig. 7). The weak reflections, however, are inclined towards the NE indicating a non-draping geometry (Fig. 7). The relationship between the different lithotypes is shown in core section B-8-2 (Fig. 5). The thickness of the individual fining-up sand successions varies between thin lamination and massive bedding with partly erosive basal contacts to the underlying clay-rich successions. Additionally, the laminated fines are sporadically intercalated by bright yellowish-beige clay laminae (LE4). The sand beds show high-density and rather low magnetic susceptibility signals, whereas the clay rich successions have a lower density, but a higher magnetic susceptibility signal. In general, the density and magnetic susceptibility profiles display mirrored patterns (Fig. 3): The density signal of the fining-up sand beds is noisier due to its variable thickness and occurrence of clay laminations. However, several of them show strong magnetic susceptibility peaks, likely caused by a higher mica content. Below 12 mcd, bSi is considered absent based on smear slide inspection. Organic matter concentration is very low (<0.5%wt). Varying but generally low CaCO$_3$ contents occur in the coarse beds and higher values where fines predominate. The Cc/Dol ratio shows varying values in the upper half of the section with a peak at around 17 mcd and low ones below, due to the low number of samples, not robust correlation with the lithotypes was possible. The Si/Ti-ratio is elevated in the coarse beds and low in the fines. Fining-up coarse beds show intermediate values. Overall, the Si/Ti curve matches well with the density curve (Figs. 3 and 4). The Zr/Ti-ratio has a noisy pattern, but the coarser sand beds present a high-amplitude and high-frequency signal, whereas the clay-dominated beds show lower values.

4 Discussion: paleoenvironmental evolution

The 24-m recovered sediment ssequence documents the postglacial evolution of Lake Constance during the last ~14 ka. The lowermost stratigraphic unit, Unit 3, contains sediments from the late Bølling–Allerød interstadial to the late Younger Dryas stadial (Fig. 6). The period represents the last 'cold' state of the lake region with low productivity and a depositional environment characterized with the sedimentation of predominantly clastic detritus. Even though, the Bølling–Allerød was characterized in previous cores from Lake Constance (Wessels, 1998b) and in other lakes in the northern perialpine realm by increased biological productivity (Ammann et al., 2013), Unit 3 shows only few samples with enhanced organic matter content not exceeding 1% (Fig. 4). In addition, the carbonates in this section are detrital as supported by microscopic analysis. Overall, the entire unit was rather quickly deposited with over 12.6 m in just ~2 ka. The two endmember lithotypes of this unit, LB7 and LE7, represent two very different depositional patterns. The laminated fine-grained deposits, LB7, are interpreted as pelagic-lacustrine, potentially varved, background deposits, while the abundant siliciclastic dominated coarse-grained sand beds, LE7, represent high-energy periods when coarse particles were transported dynamically into the deep basin. The frequent alternations between those two depositional modes indicate a highly dynamic sedimentological environment with locally highly varying sedimentation rates.

(i) Laminated fine-grained successions (LB7): The beige-yellowish fine-grained laminated succession show a higher carbonate content and represent a mixture of the averaged low-energy sediment influx into the entire lake. They were previously identified in other sediment cores from Lake Constance and other perialpine lakes as background deposits, including in the prominent bright yellowish layers (LE4 in Table 2; Hanisch et al., 2009; Niessen et al., 1992; Schwalb et al., 2013; Wessels, 1995, 1998b).

(ii) Coarse-grained siliciclastic sandy successions (LE7): Each up to ~1 m thick sand bed was most likely deposited during a single event of short duration (hours to days). In contrast to the fine-grained deposits, the sand source has to be of a more local origin and fed from the northern lake shore as the drilling location is located on the northwestern slope of the deep basin. This local signal is also supported by previous sediment-core studies that documented lithological equivalent units (Table 5) for the laminated background sediments, but not for the sands (Hanisch et al., 2009; Schwalb et al., 2013; Wessels, 1995, 1998b). The increased siliciclastic contents (Fig. 4), the greater grain size, the increased thickness of the individual deposits and consequently the increased sedimentation rate compared to the background sedimentation indicate a much higher depositional energy. The bathymetric data clearly document the presence of a subaqueous, branched to meandering channel system characterized by multiple branches originating in the Seefelder Aach Delta to the northwest. The traces of the channel systems are still visible on today's lake floor through the >10 m thick Holocene drape (Fig. 8).This highly dynamic system producing two endmember lithologies, which are controlled by the distance to the active paleochannels: LE7 within or very proximal to the channel and LB7 as the background sedimentation in inactive and unaffected parts of the channel. The channel system can be traced back into the Seefelder Aach Delta, but the present stream delivers only few m³/s of water, which is not sufficient to generate such deeply incised channels and the associated overbank deposits. It must have been formed by a Late Glacial stream with higher discharge rates and

Table 5 Correlation of the stratigraphic units from the HIBO19-Core with previous stratigraphic units from Wessels (1995, 1998a, b), Hanisch et al. (2009), and Schwalb et al. (2013)

| Lithotype corelation			
Wessels (1995, 1998a, b)	**Hanisch et al. (2009)**	**Schwalb et al. (2013)**	**HIBO19**
Turbidites, massive sands, and laminated silts	Unit 5	Unit 4	Unit 1a and 1b
Light brown to dark grey laminated silt	Unit 4/4a	Unit 3	Unit 1c and 1d
Black spotted lake marls	Unit 3	Unit 2	Unit 2
Massive, brownish grey to dark grey muds	Unit 2		
Yellowish brown to grey rhythmites	Unit 1	Unit 1	Unit 3
Deformed sandy and gravelly mud	Not recovered	Not recovered	Not recovered
Laminated grey muds			
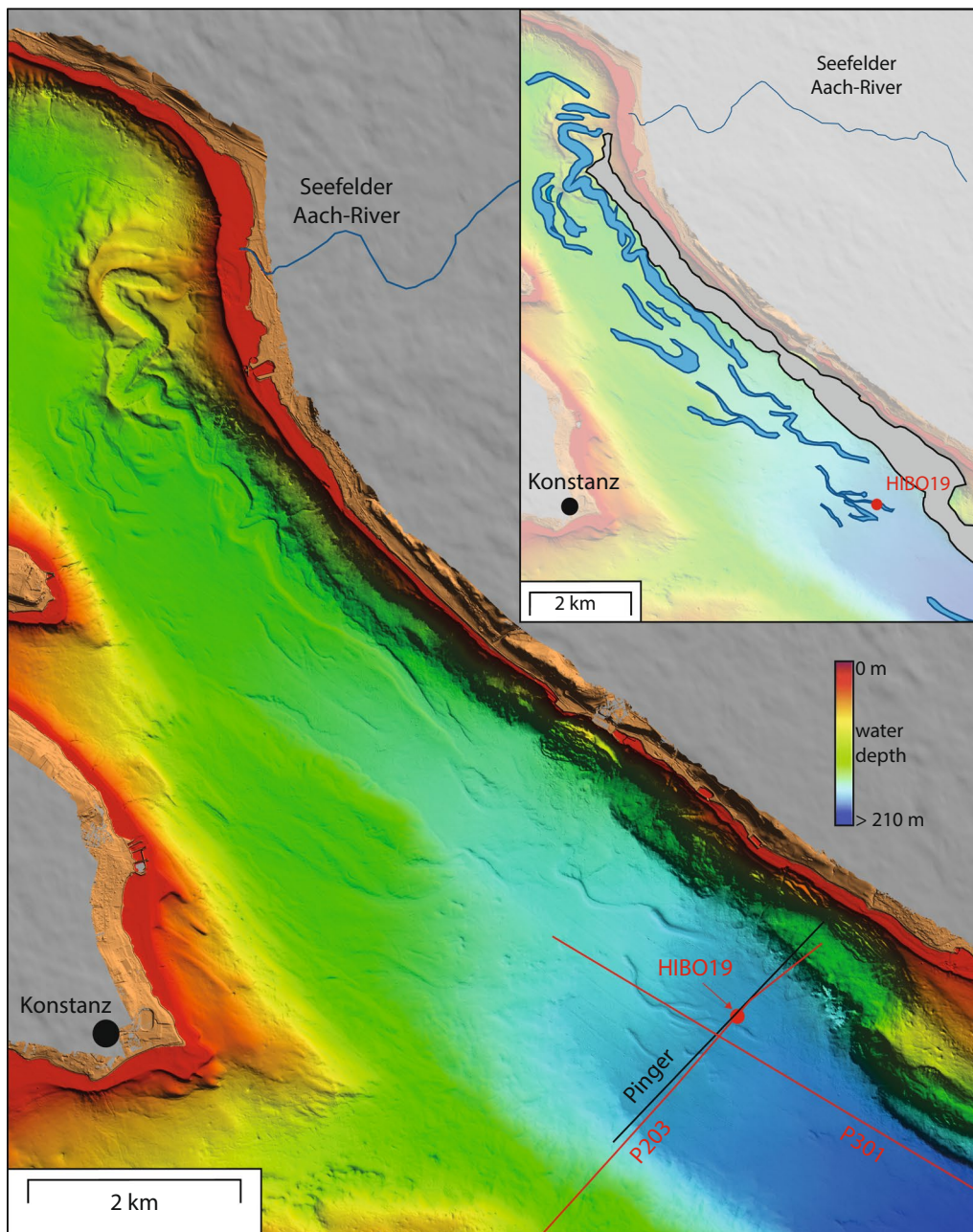
Fig. 8 Detailed bathymetric map around the coring site and the Seefelder-Aach River. The two airgun seismic lines and the coring site (WGS84: 47.66813°/9.28686°) are marked in red and the high resolution pinger line in black, the City of Konstanz shown as black dot and the Aach River in blue. The yellow ochre colored area along the shoreline is based on LIDAR-data for elevations between 0 and 1 m above the reference lake level of 395 m a.s.l. (Wessels et al., 2015). The inset on the upper right illustrates prominent geomorphological features, such as subaquatic canyons, highlighted in light blue and potential source areas of subaquatic mass movements in light grey

suspension load that was active until the Younger-Dryas-Holocene-transition after which the major sand deposits are absent in the cores. A potential sand source would be the mobilized glaciofluvial sediments of t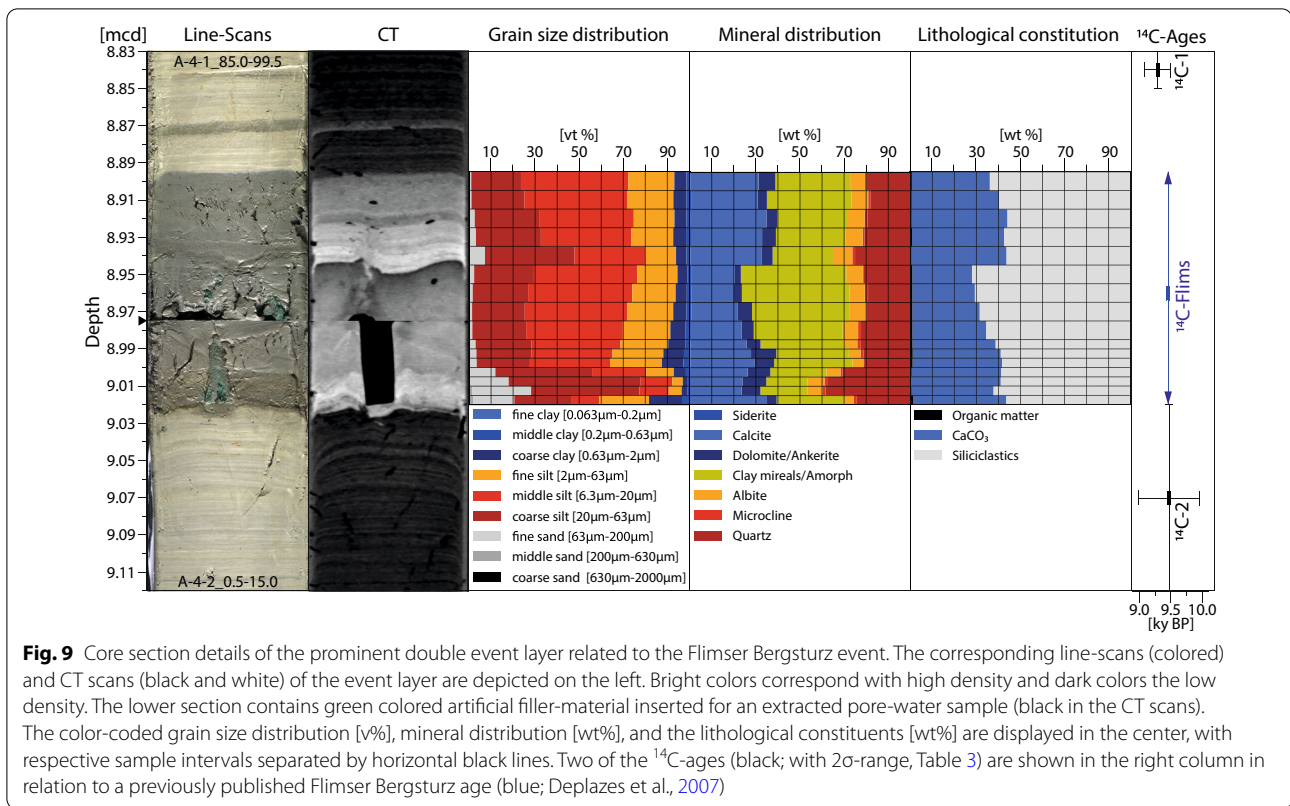he retreating Rhine Glacier. How-ever, it is assumed that the glacier has retreated latest around 17 ka BP back into the Alpine valleys to the south (Gaar et al., 2019; Wessels, 1998b). A direct link to meltwater escaping a retreating gla-cier lobe is thus very unlikely. Nevertheless, the

glacier may have provided easily erodible deposits in the proglacial environment (i.e., sander plain without vegetation) in the catchment area. These deposits might have been remobilized by the Late Glacial Seefelder Aach River and were fed into the erosive channel system. Alternatively, the sands may also represent eroded molasse bedrock by the Aach River (e.g., Aachtobel), a bedrock source that requires, however, higher runoff as the previously proposed mobilization mechanism for Late Glacial sediments. A mix of both sources might also have contributed to the deposition of the coarse-grained deposits in the lake basin. In any case, the required runoff values are not easy to be reached once the Rhine Glacier has retreated from the northern shore. A possible explanation to generate the required high-discharge events could be outburst events from breaching dams, such as outbreaks of moraine dammed lakes in the catchment of the Aach River. Such lakes possibly existed during deglaciation (Keller & Krayss, 2000), however, they may have also been present until the end of the Late Glacial and their runoffs might have kept the channel system active.

Unit 2 represents the Younger-Dryas–Holocene-transition, when a clear change in the paleoenvironmental setting occurred. The massive sands and the beige-yellowish clays disappear and are replaced by a beige-grey silty mud void of organic matter and siliceous algal remains (Fig. 4). The entire unit has been deposited rather quickly, 1.42 m in ~0.8 ka, but still much slower than the underlying Unit 3. The homogeneous lower part of Unit 2 was deposited during a stable, calm, and low-energy phase, which was replaced by a more unstable depositional phase represented by the thin sand layers. These layers are potential traces of minor reactivation phases of the channel system. They are intercalated by several homogeneities, that can likely be linked to subaquatic mass movements as their traces are still visible in the bathymetric data (Fig. 8). The top of Unit 2 is formed by a mud-clast conglomerate overlying a normal-graded bed. They both must have been formed by the major mass movement with thick deposits identified on the high-resolution seismic line towards the NE (blue mm; Fig. 7) and not necessarily by an event going down the channel system, in particular as the lake floor was already levelled out by then (Fig. 7). The subaquatic mass movement from the steep slopes first triggered a high-velocity turbidite flow transporting and depositing the sand that became eventually overlain by the mud-clast conglomerate indicating a slower debris-flow-like process eroding and mobilizing the previously deposited yellowish-beige and grey clasts.

Unit 1 represents the Holocene sediments that were deposited when the lake changed to a higher trophic state. The depositional environment became stable and low-energy conditions prevailed, as documented in the laminated to layered background sediments. Sedimentation rate decreased to <1 m/ka (~10 m in ~11 ka). The age-depth model indicates for Subunit 1d an even lower sedimentation rate during the early phase of the warming lake (~0.65 m/ka). The predominating stable and low-energy conditions of Unit 1 were only disturbed upon few occasions: (i) cm-scaled sand beds in Subunit 1d with terrestrial macro remains indicating a terrestrial source of these clastic layers that are related to high-discharge events from reactivated channel phases by the Seefelder Aach or from remobilization of near-shore deposits through lateral mass movements causing turbidity currents; (ii) turbiditic and partly homogenite-like event layers that occur frequently until the transition of Subunits 1c to 1b; and (iii) minor fine-grained event layers in Subunit 1a and b that are related with slightly increased runoffs during floods and heavy rainfalls.

The major and most prominent disturbance of the low-energy environment is represented by the two thickest and coarsest turbiditic event layers in Unit 1 at 8.895–9.025 mcd (Fig. 9). Age data and comparison to previous studies (Schneider et al., 2004) connect this layer to the Flimser Bergsturz, the largest rockslide in the Alps that occurred ~9.5 ky BP over 100 km upstream the Rhine River (Deplazes et al., 2007; Poschinger, 2005). The ^{14}C-dates of the over and underlying background deposits (Fig. 9) corresponds well with the postulated age of the Flimser Bergsturz of 9480–9430 cal. BP (Deplazes et al., 2007). The grain-size distribution, the mineral-phase distribution, the lithological constitution, and the CT scans of the layer clearly reveal the two-phased character with two stacked normally graded beds of ~5 (upper) and ~7 (lower) cm thickness within this anomaly. Upward decreasing carbonate contents in the graded beds may reflect a grain size effect (increasing clay content up-core). Additionally, the CT scans reveal a ~1–2 mm thick low-density layer in between these two turbiditic layers (Fig. 9). This thin layer represents the background period before the secondary event occurred, supporting the postulated short time period in between the two events (Schneider et al., 2004). Furthermore, the two bases, especially the lower one, are clearly of a wavy shape, as is typical for hyperpycnal flood events (Mulder & Alexander, 2001; Zavala, 2020), an interpretation supported by the matching peaks in the grain-size distribution as well as quartz and feldspar content. Carbonate content shows the highest concentrations measured in coarser detrital deposits, i.e., >40% in comparison to ~20–25% in the sand deposits in Unit 3. Consequently, these two stacked

Fig. 9 Core section details of the prominent double event layer related to the Flimser Bergsturz event. The corresponding line-scans (colored) and CT scans (black and white) of the event layer are depicted on the left. Bright colors correspond with high density and dark colors the low density. The lower section contains green colored artificial filler-material inserted for an extracted pore-water sample (black in the CT scans). The color-coded grain size distribution [v%], mineral distribution [wt%], and the lithological constituents [wt%] are displayed in the center, with respective sample intervals separated by horizontal black lines. Two of the ^{14}C-ages (black; with 2σ-range, Table 3) are shown in the right column in relation to a previously published Flimser Bergsturz age (blue; Deplazes et al., 2007)

turbidites require a source area that is richer in mobile carbonates. This can be explained by the redeposits of the 9 km^3 of rockslide material provided by the Flims event (Poschinger, 2005). An initial explanation for the two-phased characteristic appearance of the event layer in Lake Constance was provided by Schneider et al. (2004) interpreting the lower layer as Flimser Bergsturz and the upper layer as Taminser Bergsturz signal, a temporal succession not anymore supported by recent investigations in the Flims/Tamins rockslide area (Calhoun et al., 2015; Poschinger, 2005). A more likely interpretation is that the lower layer is a direct result of the Flimser Bergsturz that mobilized, in addition to the falling rock masses, an enormous amount of Quaternary valley-fill deposits, while the upper layer represents the remains of an outburst of the rockslide-dammed Lake Ilanz a few years after the rock slide (Poschinger, 2005). In fact, a third carbonate-rich but thinner (5 mm thick) turbidite 2 cm above the upper layer (8.87–8.875 mcd; Fig. 9) might represent a later outburst event upon a further incision and lowering of the dam.

The entire Holocene unit is marked by a shift in sediment composition (Fig. 3) and by a change in depositional mechanism. In Subunit 1d, productivity increases up core leading to precipitation of endogenic calcite as indicated by microscopic analysis of shape, size, and interference colors, which is further supported by the exceptionally high calcite concentrations and Ca/Ti-ratio (Fig. 4). CaCO$_3$ content decreases substantially up-core from the middle of Subunit 1d until the end of 1b, while organic matter and bSi contents remain stable. Additionally, the sediment composition changes again from one dominated by autochthonous constituents to one that is dominated by allochthonous clastic material. It is, however, not entirely clear if this shift was caused by increased allochthonous input or by a decrease in autochthonous flux (Wessels, 1998b). The increased sediment flux of the Rhine as an explanation for the changes is supported by: (i) the increased occurrence of turbidites, (ii) the lower sedimentation rate of Subunit 1d compared to Unit 1; and (iii) the strong upsurge in siliciclastic sedimentation and declining Ca/Ti-ratios. The very top of the Holocene sediments, Subunit 1a, represents a rapid shift in the paleoenvironment: highly elevated carbonate, organic matter, and bSi contents, together with the black color of the laminas, indicate anthropogenically-induced eutrophication of Lake Constance during the late Holocene (Wessels et al., 1999).

5 Summary and conclusions

The 24-m-long sediment core (HIBO19) recovered from the deep basin of Lake Constance in over 200 m water depth provides a nearly continuous sediment record reflecting the environmental history since the Late Glacial. With a bottom age of ~13.7 ka BP, the base of the record reaches back into the Bølling–Allerød interstadial and offers a high-resolution insight into the post-glacial evolution of the lake. Late Glacial sediments document a very low lake productivity and a high-variability depositional environment due to local hydrodynamic conditions which typical of a proglacial cold lake. The low-energy phases are represented by the finely laminated background clay deposits, whereas the sand particles were transported to the coring site with episodic high-energy hyperpycnal flows through an impressive subaquatic channel system. Geomorphological channel routing analysis identified the Seefelder Aach River Delta on the northern shore of Lake Constance as the most likely source of the sand. Since the Rhine Glacier had already retreated from Lake Constance Basin at the time of deposition, the glacier itself could not have been the direct source of the sand. Instead, the sand may have been remobilized from sander outwash plains deposited in the River Aach-catchment by the retreating Rhine Glacier, or it may have originated from eroded molasse bedrock. The observed deposition of coarse layers requires high-discharge flow events capable of transporting large amounts of sands and pouring them to the deep-water realm, which cannot be achieved by the modern low-energy river system. One hypothesis is that these high-discharge events may be related to the collapse of moraine-dammed meltwater lakes in the catchment north of Lake Constance that persisted until the end of the Late Glacial, provoking major outburst floods. However, the circumstances of the formation and deposition of these sands cannot be conclusively clarified based on the available data, which, in contrast to the well-known laminated background sediments, are only known from the HIBO19-cores. The same applies to a mud-clast conglomerate, which was deposited at the end of the Younger Dryas stadial and probably represents the distal effect of a subaquatic mass movement as identified at the toe-of-slope on the seismic data. This fact underlines the uniqueness of observing these sands and the need of drilling deep into these pre-Holocene sediments to gather detailed information that cannot be obtained only by seismic or other geophysical surveys. Therefore, the close linking of high-resolution seismic surveys with sedimentological investigations of several long cores recovered from the channel system, covering the whole transect from its roots to its end, could contribute to a better understanding of the formation mechanism of the system. Additionally, drilling through the whole post-glacial succession, which contains the complete channel dominated sequence, would help to reconstruct, and date the evolution of the system.

A major change in the depositional environment occurred at the Younger-Dryas–Holocene-transition, which marks the onset of a modern warm lake with increased biotic productivity. The whole Holocene record shows dominant, stable low-energy and deep-water conditions. However, the records reveal phases of higher energy and rapid deposition during the early Holocene, represented by homogenites and cm-scaled sand layers that might be associated with minor reactivation phases of the subaquatic channel system or with lateral mass movements producing turbidites. During the mid-Holocene, the frequency of brownish, fining up turbiditic layers, representing local flood events, increases. The most prominent Holocene event is the dm-scaled double turbidite coinciding with the Flimser Bergsturz, the largest Alpine rockslide that occurred ~100 km upstream the Rhine-river. Framing ^{14}C-ages of the event layer coincide well with the established event ages of 9480–9430 cal. BP for the Flimser Bergsturz. While the lower layer might be a direct product of the rockslide itself, the upper turbidite and a third, much thinner turbidite above, might result from a dam breach of the rockslide-dammed Lake Ilanz. More cores, in particular from the deep-water depocenter of Lake Constance, are required to increase confidence of these interpretations.

A shift from in-situ carbonate production to an allochthonous siliciclastic dominated sedimentation occurred in late early-Holocene (~7–8 ka BP). This shift might be correlated with an increased sediment influx from the Rhine or with a decrease in the in-situ carbonate production. The lake was dominated by allochthonous siliciclastic sedimentation until very recent times, when the carbonate, organic matter, and bSi contents dramatically increased during the anthropogenic eutrophication of Lake Constance. This late phase in the lake evolution with increased nutrient supply is represented by the uppermost black and organic-rich sediments.

Supplementary Information

 Additional file 1: Table S1. Optical stimulated luminescence dating data summary (OSL-IR50 and pIR150) and additional information.

Additional file 2: Figure S1. Overview of core section recovered from three logs (Core A, B, C) from Lake Constance and reconstructed composite section, conversion between mcd and cmsd, estimated core losses reconstructed from the composited depth.

Declarations

Author details

[1]Institute of Geological Sciences and Oeschger Centre of Climate Change Research, Universität Bern, Baltzerstrasse 1+3, 3012 Bern, Switzerland. [2]Geochemistry & Isotope Biogeochemistry, Leibniz Institute for Baltic Sea Research (IOW), Seestrasse 15, 18119 Warnemünde, Germany. [3]Marine Geochemistry, University of Greifswald, Friedrich-Ludwig-Jahn Str. 17a, 17489 Greifswald, Germany. [4]Department of Maritime Systems, Interdisciplinary Faculty, University of Rostock, Albert-Einstein-Str. 21, 18059 Rostock, Germany. [5]Limnologisches Institut, Universität Konstanz, Mainaustraße 252, 78464 Constance, Germany. [6]Helmholtz Centre Potsdam, GFZ German Research Centre for Geosciences, Telegrafenberg, 14473 Potsdam, Germany. [7]Institut für Geowissenschaften, Christian-Albrechts-Universität zu Kiel, Olshausenstrasse 40, 24118 Kiel, Germany. [8]Institute of Geosystems and Bioindication, Technische Universität Braunschweig, Langer Kamp 19c, 38106 Brunswick, Germany. [9]Institut für Seenforschung (ISF) der Landesanstalt für Umwelt Baden-Württemberg (LUBW), Argenweg 50, 88085 Langenargen, Germany.

References

Akker, I. V., Berger, A., Zwingmann, H., Todd, A., Schrank, C. E., Jones, M. W. M., Kewish, C. M., Schmid, T. C., & Herwegh, M. (2021). Structural and chemical resetting processes in white mica and their effect on K-Ar data during low temperature metamorphism. *Tectonophysics, 800*, 228708. https://doi.org/10.1016/j.tecto.2020.228708

Ammann, B., von Grafenstein, U., & van Raden, U. J. (2013). Biotic responses to rapid warming about 14,685yr BP: Introduction to a case study at Gerzensee (Switzerland). *Palaeogeography, Palaeoclimatology, Palaeoecology, 391*, 3–12. https://doi.org/10.1016/j.palaeo.2013.11.006

Auclair, M., Lamothe, M., & Huot, S. (2003). Measurement of anomalous fading for feldspar IRSL using SAR. *Radiation Measurements, 37*(4–5), 487–492. https://doi.org/10.1016/S1350-4487(03)00018-0

Böttcher, M. E., Neubert, N., Escher, P., von Allmen, K., Samankassou, E., & Nägler, T. F. (2018). Multi-isotope (Ba, C, O) partitioning during experimental carbonatization of a hyper-alkaline solution. *Geochemistry, 78*(2), 241–247. https://doi.org/10.1016/j.chemer.2018.01.001

Buechi, M. W., Graf, H. R., Haldimann, P., Lowick, S. E., & Anselmetti, F. S. (2018). Multiple quaternary erosion and infill cycles in overdeepened basins of the northern Alpine foreland. *Swiss Journal of Geosciences, 111*(1–2), 133–167. https://doi.org/10.1007/s00015-017-0289-9

Calhoun, N., Poschinger, A. V., Clague, J. J., Giardino, M., Masera, D., & Perotti, L. (2015). New pieces to the flims-tamins rockslide puzzle. In D. Giordan, G. B. Crosta, J. Corominas, R. Azzam, J. Wasowski, N. Sciarra, & G. Lollino (Eds.), *Engineering geology for society and territory—Volume 2* (pp. 899–903). Springer. https://doi.org/10.1007/978-3-319-09057-3_155

Colarossi, D., Duller, G. A. T., Roberts, H. M., Tooth, S., & Lyons, R. (2015). Comparison of paired quartz OSL and feldspar post-IR IRSL dose distributions in poorly bleached fluvial sediments from South Africa. *Quaternary Geochronology, 30*, 233–238. https://doi.org/10.1016/j.quageo.2015.02.015

Croudace, I. W., & Rothwell, R. G. (2015). *Micro-XRF studies of sediment cores: Applications of a non-destructive tool for the environmental sciences* (Vol. 17). Springer Netherlands. https://doi.org/10.1007/978-94-017-9849-5

Deplazes, G., Anselmetti, F. S., & Hajdas, I. (2007). Lake sediments deposited on the Flims rockslide mass: The key to date the largest mass movement of the Alps. *Terra Nova, 19*(4), 252–258. https://doi.org/10.1111/j.1365-3121.2007.00743.x

Durcan, J. A., King, G. E., & Duller, G. A. T. (2015). DRAC: Dose rate and age calculator for trapped charge dating. *Quaternary Geochronology, 28*, 54–61. https://doi.org/10.1016/j.quageo.2015.03.012

Fabbri, S. C., Affentranger, C., Krastel, S., Lindhorst, K., Wessels, M., Madritsch, H., Allenbach, R., Herwegh, M., Heuberger, S., Wielandt-Schuster, U., Pomella, H., Schwestermann, T., & Anselmetti, F. S. (2021). Active faulting in Lake Constance (Austria, Germany, Switzerland) unraveled by multi-vintage reflection seismic data. *Frontiers in Earth Science, 9*, 670532. https://doi.org/10.3389/feart.2021.670532

Gaar, D., Graf, H. R., & Preusser, F. (2019). New chronological constraints on the timing of Late Pleistocene glacier advances in northern Switzerland. *E&G Quaternary Science Journal, 68*(1), 53–73. https://doi.org/10.5194/egqsj-68-53-2019

Galbraith, R. F., Roberts, R. G., Laslett, G. M., Yoshida, H., & Olley, J. M. (1999). Optical dating of single and multiple grains of quartz from Jinmium rock shelter, Northern Australia: Part I, experimental design and statistical models. *Archaeometry, 41*(2), 339–364. https://doi.org/10.1111/j.1475-4754.1999.tb00987.x

Hanisch, S., Wessels, M., Niessen, F., & Schwalb, A. (2009). Late Quaternary lake response to climate change and anthropogenic impact: Biomarker evidence from Lake Constance sediments. *Journal of Paleolimnology, 41*(3), 393–406. https://doi.org/10.1007/s10933-008-9232-4

Harms, U., Raschke, U., Anselmetti, F. S., Strasser, M., Wittig, V., Wessels, M., Schaller, S., Fabbri, S. C., Niederreiter, R., & Schwalb, A. (2020). Hipercorig—An innovative hydraulic coring system recovering over 60 m long sediment cores from deep perialpine lakes. *Scientific Drilling, 28*, 29–41. https://doi.org/10.5194/sd-28-29-2020

Harms, U., Schaller, S., Raschke, U., Anselmetti, F. S., Boettcher, M. E., Buechi, M. W., Epp, L. S., Fabbri, F. C., Gribenski, N., Krastel, S., Liebezeit, A., Lindhorst, K., Schleheck, D., Schmiedinger, I., Schwalb, A., Vogel, H., Wessels, M., & Wittig, V. (2021). Sedimentological, geochemical, petrophysical, and geochronological data on drill cores and samples from the 2019 Lake Constance (Germany) drilling campaign with Hipercorig. *GFZ Data Services*. https://doi.org/10.5880/fidgeo.2021.040

Hermen, F., Beaud, F., Champagnac, J. D., Lemieux, J. M., & Sternai, P. (2011). Glacial hydrology and erosion patterns: A mechanism for carving glacial valleys. *Earth and Planetary Science Letters, 310*(3–4), 498–508. https://doi.org/10.1016/j.epsl.2011.08.022

Huntley, D. J., & Lamothe, M. (2011). Ubiquity of anomalous fading in K-feldspars and the measurement and correction for it in optical dating. *Canadian Journal of Earth Sciences*. https://doi.org/10.1139/e01-013

Huuse, M. (2000). Overdeepened quaternary valleys in the eastern Danish North Sea: Morphology and origin. *Quaternary Science Reviews, 19*(12), 1233–1253. https://doi.org/10.1016/S0277-3791(99)00103-1

Ivy-Ochs, S., Kerschner, H., Reuther, A., Preusser, F., Heine, K., Maisch, M., Kubik, P. W., & Schlüchter, C. (2008). Chronology of the last glacial cycle in the European Alps. *Journal of Quaternary Science, 23*(6–7), 559–573. https://doi.org/10.1002/jqs.1202

Keller, O., & Krayss, E. (2000). Die Hydrographie des Bodenseeraums in Vergangenheit und Gegenwart. *Berichte der St. Gallischen Naturwissenschaftlichen Gesellschaft, 89*, 20. https://doi.org/10.5169/seals-832575

Keller, O., & Krayss, E. (2011). Mittel- und spätpleistozäne Stratigraphie und Morphogenese in Schlüsselregionen der Nordschweiz. *E&G Quaternary Science Journal, 59*(1/2), 88–119. https://doi.org/10.3285/eg.59.1-2.08

Keller, O., Sg, E., & Krayss, E. (2005a). Der Rhein-Linth-Gletscher im letzten Hochglazial A. *Vierteljahrsschrift Der Naturforschenden Gesellschaft in Zürich, 150*, 19–32.

Keller, O., Sg, E., & Krayss, E. (2005b). Der Rhein-Linth-Gletscher im letzten Hochglazial B. *Vierteljahrsschrift Der Naturforschenden Gesellschaft in Zürich, 150*, 69–85.

Kreutzer, S., Schmidt, C., Fuchs, M. C., Dietze, M., & Fuchs, M. (2012). Introducing an R package for luminescence dating analysis. *Ancient TL, 30*, 1–8.

Lipka, M., Woelfel, J., Gogina, M., Kallmeyer, J., Liu, B., Morys, C., Forster, S., & Böttcher, M. E. (2018). Solute reservoirs reflect variability of early diagenetic processes in temperate brackish surface sediments. *Frontiers in Marine Science, 5*, 413. https://doi.org/10.3389/fmars.2018.00413

López, G. I., Goodman-Tchernov, B. N., & Porat, N. (2018). OSL over-dispersion: A pilot study for the characterisation of extreme events in the shallow marine realm. *Sedimentary Geology, 378*, 35–51. https://doi.org/10.1016/j.sedgeo.2018.09.002

Lukas, S., Preusser, F., Anselmetti, F. S., & Tinner, W. (2012). Testing the potential of luminescence dating of high-alpine lake sediments. *Quaternary Geochronology, 8*, 23–32. https://doi.org/10.1016/j.quageo.2011.11.007

Magrani, F., Valla, P. G., Gribenski, N., & Serra, E. (2020). Glacial overdeepenings in the Swiss Alps and foreland: Spatial distribution and morphometrics. *Quaternary Science Reviews, 243*, 106483. https://doi.org/10.1016/j.quascirev.2020.106483

Meyer-Jacob, C., Vogel, H., Boxberg, F., Rosén, P., Weber, M. E., & Bindler, R. (2014). Independent measurement of biogenic silica in sediments by FTIR spectroscopy and PLS regression. *Journal of Paleolimnology, 52*(3), 245–255. https://doi.org/10.1007/s10933-014-9791-5

Meyers, P. A., & Teranes, J. L. (2001). Sediment organic matter. In W. M. Last & J. P. Smol (Eds.), *Tracking environmental change using lake sediments: physical and geochemical methods* (pp. 239–269). Springer Netherlands. https://doi.org/10.1007/0-306-47670-3_9

Mulder, T., & Alexander, J. (2001). The physical character of subaqueous sedimentary density flows and their deposits. *Sedimentology, 48*, 269–299.

National Centers for Environmental Information (NCEI). (2020). Retrieved from https://www.ncdc.noaa.gov/paleo-search/study/2481.

Niessen, F., Lister, G., & Giovanoli, F. (1992). Dust transport and palaeoclimate during the Oldest Dryas in Central Europe—Implications from varves (Lake Constance). *Climate Dynamics, 8*(2), 71–81. https://doi.org/10.1007/BF00209164

Poschinger, A. V. (2005). Der Flimser Bergsturz als Staudamm. *Bulletin Für Angewandte Geologie, 10*, 33–47. https://doi.org/10.5169/SEALS-225564

Preusser, F., Degering, D., Fuchs, M., Hilgers, A., Kadereit, A., Klasen, N., Krbetschek, M., Richter, D., & Spencer, J. Q. G. (2008). Luminescence dating: Basics, methods and applications. *E&G Quaternary Science Journal, 57*(1/2), 95–149. https://doi.org/10.3285/eg.57.1-2.5

Preusser, F., Graf, H. R., Keller, O., Krayss, E., & Schlüchter, C. (2011). Quaternary glaciation history of northern Switzerland. *E&G Quaternary Science Journal, 60*(2/3), 282–305. https://doi.org/10.3285/eg.60.2-3.06

Preusser, F., & Kasper, H. U. (2001). Comparison of dose rate determination using high-resolution gamma spectrometry and inductively coupled plasma-mass spectrometry. *Ancient TL*. https://doi.org/10.7892/BORIS.86818

Preusser, F., Reitner, J. M., & Schlüchter, C. (2010). Distribution, geometry, age and origin of overdeepened valleys and basins in the Alps and their foreland. *Swiss Journal of Geosciences, 103*(3), 407–426. https://doi.org/10.1007/s00015-010-0044-y

Reber, R., & Schlunegger, F. (2016). Unravelling the moisture sources of the Alpine glaciers using tunnel valleys as constraints. *Terra Nova, 28*(3), 202–211. https://doi.org/10.1111/ter.12211

Reimann, T., & Tsukamoto, S. (2012). Dating the recent past (< 500 years) by post-IR IRSL feldspar—Examples from the North Sea and Baltic Sea coast. *Quaternary Geochronology, 10*, 180–187. https://doi.org/10.1016/j.quageo.2012.04.011

Reimer, P. J., Austin, W. E. N., Bard, E., Bayliss, A., Blackwell, P. G., Bronk Ramsey, C., Butzin, M., Cheng, H., Edwards, R. L., Friedrich, M., Grootes, P. M., Guilderson, T. P., Hajdas, I., Heaton, T. J., Hogg, A. G., Hughen, K. A., Kromer, B., Manning, S. W., Muscheler, R.,…, Talamo, S. (2020). The IntCal20 northern hemisphere radiocarbon age calibration curve (0–55 cal kBP). *Radiocarbon, 62*(4), 725–757. https://doi.org/10.1017/RDC.2020.41

Schneider, J.-L., Pollet, N., Chapron, E., Wessels, M., and Wassmer, P., 2004, Signature of Rhine Valley sturzstrom dam failures in Holocene sediments of Lake Constance, Germany: Sedimentary Geology, v. 169, p. 75–91, doi:https://doi.org/10.1016/j.sedgeo.2004.04.007.

Schwalb, A., Dean, W., Güde, H., Hanisch, S., Sobek, S., & Wessels, M. (2013). Benthic ostracode δ13C as sensor for early Holocene establishment of modern circulation patterns in Central Europe. *Quaternary Science Reviews, 66*, 112–122. https://doi.org/10.1016/j.quascirev.2012.10.032

Schwestermann, T. (2016). *Mass-movement event stratigraphy in Lake Constance. (MSc Thesis), ETH Zürich*, pp. 90

Taubner, H., Roth, B., & Tippkötter, R. (2009). Determination of soil texture: Comparison of the sedimentation method and the laser-diffraction analysis. *Journal of Plant Nutrition and Soil Science, 172*(2), 161–171. https://doi.org/10.1002/jpln.200800085

Vogel, H., Meyer-Jacob, C., Thöle, L., Lippold, J. A., & Jaccard, S. L. (2016). Quantification of biogenic silica by means of Fourier transform infrared spectroscopy (FTIRS) in marine sediments: Quantification of biogenic silica. *Limnology and Oceanography: Methods, 14*(12), 828–838. https://doi.org/10.1002/lom3.10129

Wessels, M. (1995). Bodensee-Sedimente als Abbild von Umweltänderungen im Spät- und Postglazial. *Göttinger Arb. Geol. Paläont, 66*, 1–105.

Wessels, M. (1998a). Geological history of Lake Constance area. In: Bäuerle, E. & Gaedke, U.: *Lake Constance. Characterization of an ecosystem in transition. Archiv Hydrobiol* (Vol. 53, pp. 1–12)

Wessels, M. (1998b). Late-glacial and postglacial sediments in Lake Constance (Germany) and their palaeolimnological implications. In: Bäuerle, E. & Gaedke, U.: *Lake Constance. Characterization of an ecosystem in transition. Archiv Hydrobiol* (Vol. 53, pp. 411–449)

Wessels, M. (1998c). Natural environmental changes indicated by Late Glacial and Holocene sediments from Lake Constance, Germany. *Palaeogeography, Palaeoclimatology, Palaeoecology, 140*, 421–432.

Wessels, M., Anselmetti, F. S., Artuso, R., Baran, R., Daut, G., Gaide, S., Geiger, A., Groenveld, J. D., Hilbe, M., Möst, K., Klauser, B., Niemann, S., Roschlaub, R., Steinbacher, F., Wintersteller, P., & Zahn, C. (2015). Bathymetry of Lake Constance—a high-resolution survey in a Large, Deep Lake. *Zfv – Zeitschrift Für Geodäsie, Geoinformation Und Landmanagement*. https://doi.org/10.12902/zfv-0079-2015

Wessels, M., Mohaupt, K., Kummerlin, R., & Lenhard, A. (1999). Reconstructing past eutrophication trends from diatoms and biogenic silica in the sediment and the pelagic zone of Lake Constance, Germany. *Journal of Paleolimnology, 21*, 171–192. https://doi.org/10.1023/A:1008080922586

Zavala, C. (2020). Hyperpycnal (over density) flows and deposits. *Journal of Palaeogeography*. https://doi.org/10.1186/s42501-020-00065-x

Publisher's Note